Received: 9 March 2020 | Revised: 21 July 2020 | Accepted: 21 July 2020

DOI: 10.1111/jace.17402

Journal of the American Ceramic Society

ORIGINAL ARTICLE

Designing environment-friendly chromium-free Spinel-Periclase-Zirconia refractories for Ruhrstahl Heraeus degasser

Somnath Mandal[1,2] | **C. J. Dileep Kumar**[3,4] | **Devendra Kumar**[2] | **Komal Syed**[1] | **Marie-Aline Van Ende**[5] | **In-Ho Jung**[5] | **Sarah C. Finkeldei**[1,6] | **William J. Bowman**[1]

[1]Department of Materials Science and Engineering, University of California, Irvine, CA, USA

[2]Department of Ceramic Engineering, Indian Institute of Technology (Banaras Hindu University), Varanasi, India

[3]TRL Krosaki Refractories Limited, Belpahar, India

[4]Calderys India Refractories Limited, Katni, India

[5]Department of Materials Science and Engineering, Research Institute of Advanced Materials, Seoul National University, Seoul, South Korea

[6]Department of Chemistry, University of California, Irvine, CA, USA

Correspondence
Somnath Mandal, Department of Materials Science and Engineering, University of California, Irvine 92697, CA, USA.
Email: smnthmndl@gmail.com

Funding information
Ministry of Human Resource Development, Government of India; Science and Engineering Research Board, Government of India; ASTM International; The Refractories Institute; University of California, Irvine; NSF, Grant/Award Number: DMR 1611457

Abstract

Ruhrstahl Heraeus (RH) degassers are globally used to manufacture vacuum-treated steel for automotive and railroad applications. The state-of-the-art environment-friendly chromium-free alternatives for direct-bonded magnesia-chrome refractories used in RH degassers are expensive, and the scientific literature lacks direct correlation between materials chemistry, processing, and functional properties. We have designed a novel spinel-periclase-15 wt% ZrO_2 composition containing 14 wt% in situ spinel which exhibited 7.2 MPa hot modulus of rupture (1500°C), exceeding all reported Cr-free refractories for RH degasser applications. Investigation with scanning electron microscopy coupled with energy dispersive spectroscopy (SEM-EDS) attributed this improvement to a reduction in interparticle Ca and Si content which forms low-melting phases, as supported by FactSage thermodynamic simulations. The spinel-periclase composition SP exhibited superior thermal shock resistance because thermal shock-induced cracks were stopped by fracture porosity around MgO particles, formed due to thermal expansion mismatch. SEM-EDS analysis of the SP composition corroded by RH slag at 1650°C revealed that Fe is the most corrosive element followed by Ca and Si. Contradicting the consensus, it was observed that corrosion resistance of fused MgO was better than that of ZrO_2. The cubic ZrO_2 phase reduced FeO_x penetration locally by incorporating CaO from the RH slag into a solid solution and forming a $CaZrO_3$ phase creating a "slag barrier". Lastly, pore size was found to greatly exacerbate slag penetration following the Washburn percolation model.

KEYWORDS

corrosion/corrosion resistance, magnesium oxide, refractories, spinels, thermal shock/thermal shock resistance

1 | INTRODUCTION

The Ruhrstahl Heraeus (RH) degasser (Figure 1) is the globally preferred equipment to manufacture high quality vacuum treated steel purified to ppm level of C, H, and N.[1-3] Examples of such steel are ultra-low carbon steel (<30 ppm C) for lightweight automobile applications, high carbon manganese steel (<1.5 ppm H_2, <40 ppm N_2) for crack resistant railway tracks and electrical steel for transformer cores. Faster operation and the ability to perform gas removal, decarburization, desulphurization, and alloy addition with precise composition control makes RH degassers superior to other metallurgical equipment like the vacuum arc degasser. This paper explores refractories for use in a RH degasser which is used to manufacture steel consumed primarily by the automotive industry, one of the world's largest industries in terms of revenue. The automotive steel market is worth US$

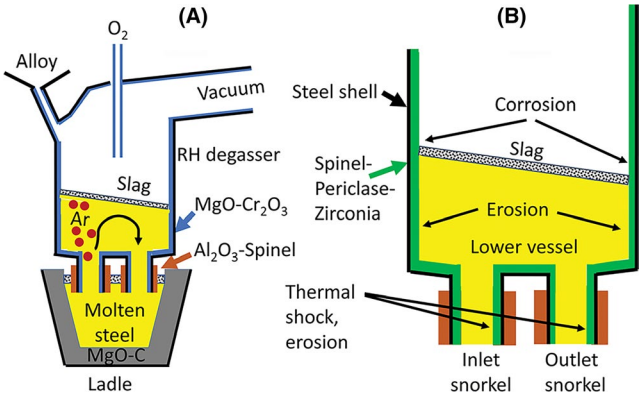

FIGURE 1 A, Schematic representation of a Ruhrstahl Heraeus degasser with direct-bonded $MgO-Cr_2O_3$ bricks in operation and (B) an enlarged image of lower vessel and snorkels showing region-specific wear mechanisms. Green colored region indicates proposed area of application of spinel-periclase-zirconia refractories which have been investigated in this study

104 billion[4] which is 4% of the global steel industry valued at US$ 2500 billion.[5] Refractory ceramics[6] for high temperature application are a US$ 25 billion industry[7] which is significant compared to the size of the lithium ion battery industry valued at US$ 37 billion.[8] Refractories are primarily manufactured in the European Union, North America, and the Asia Pacific region with 70% of their consumption in the iron and steel industry. Refractories used in the lower vessel and snorkel interior of RH degassers suffer erosion due to contact with rapidly moving molten steel (100-150 metric ton/min) at 1480-1630°C and FeO-rich corrosive slag. The inlet snorkel suffers severe abrasion due to argon gas injection. Additionally, hour-long intervals of cooling between operation cause thermal shock damage (ΔT = 800-900°C). Direct-bonded magnesia-chrome ($MgO-Cr_2O_3$, DBMC) refractory containing 18-28 wt% Cr_2O_3 is most suited for this application because it is dense (apparent porosity 11%-18%), has a high hot modulus of rupture (HMOR) of 4-9 MPa at 1500°C and has superior resistance to corrosion and thermal shock damage.[3,9-15] Water soluble Cr^{6+}-containing chromates formed in DBMC bricks during operation are carcinogenic and a skin irritant, which not only exposes maintenance and installation workers to health hazards but also can create long-term ground water pollution when disposed of into landfills.[16-21]

During the last two decades several experiments were conducted to develop environment-friendly chromium-free refractories for RH degassers, but the unique combination of vacuum environment with oxygen blowing, thermal shock, contact with fast circulating steel, and highly corrosive FeO-rich slag creates daunting challenges.[10-12,15,22-24] For example, magnesia-carbon refractories are known for their high corrosion resistance due to the large contact angle of graphite with molten slag, but oxygen blowing inside RH degassers oxidizes the carbon present in the refractory causing premature erosion.[11,23] Moreover, carbon from the magnesia-carbon refractory leaches into molten steel making it harder to produce ultra-low carbon steel (<30 ppm C). Compared to DBMC, magnesia-yttria brick has comparable properties but is expensive, and magnesia-spinel-yttria has poor HMOR.[22] These refractories were promising because Y_2O_3 can react with CaO, SiO_2, and Al_2O_3 of the slag forming high melting point reaction products like yttrium aluminum garnet (melting temperature, T_m is 1919 °C).[25] Magnesia-zirconia bricks have half the HMOR of DBMC,[22,23] and magnesia-hercynite ($MgO-FeAl_2O_4$) bricks have overall inferior properties.[12] Magnesia-alumina-titania bricks have been commercialized and have the advantage of better thermal shock resistance, similar HMOR and corrosion resistance compared to DBMC, but are expensive.[10,12,15,25] Although spinel-periclase refractories successfully replaced DBMC bricks in cement rotary kilns[26] and their high thermal shock resistance is also beneficial in RH degassers, their poor HMOR[10] will be a limitation because of higher operating temperatures and fast steel circulation.

In this paper, we design a composition for environment-friendly spinel-periclase refractory bricks to enhance their HMOR and corrosion resistance, while maintaining good thermal shock resistance for application in the lower vessel and snorkel interior of RH degassers. The mechanism of failure of refractories varies considerably in different parts of the RH degasser. For the lower vessel and snorkel interior, the decreasing order of importance of failure mechanism is: (a) erosion due to rapid molten steel circulation and abrasion due to trajectory of argon bubbles; (b) corrosion due to penetration of molten slag and steel; and (c) thermal shock (Figure 1).[24] These failure modes are directly related to refractory properties like HMOR, corrosion resistance, and thermal shock resistance. The impact of ZrO_2 addition, which is known to enhance HMOR,[27]thermal shock resistance,[28,29] and corrosion resistance,[25,30,31] is also studied and correlated with microstructure analysis and mineral phase composition using scanning electron microscopy coupled with energy dispersive spectroscopy (SEM-EDS). Thermodynamic equilibrium calculations were used to validate the phase analysis by X-ray diffraction (XRD) and the chemical microanalysis by SEM-EDS.

2 | EXPERIMENTAL METHODS AND MATERIALS DESIGN APPROACH

2.1 | Raw material selection for optimized RH degasser performance

To improve HMOR and density of the spinel-periclase (SP) composition, the following approaches were used: (a)

increased in situ spinel content from the usual 5-8 wt%[32] employed in magnesia-spinel refractory bricks to 14 wt% through the reaction of 10 wt% calcined alumina powder (HGRM 30; Hindalco, 50 vol% pass particle size, $d_{50}$is 4.7 μm) and 4 wt% sintered magnesia powder (UBE 98HD; UBE minerals; 80 μm grain size); (b) nucleate in situ spinel by holding at 1300°C for 0.5 hours[33] and finally sinter at 1700°C for 2 hours; and (c) use sintered magnesia-rich spinel (MR66 Spinel; Almatis Alumina Pvt Ltd; 20 μm grain size)instead of stoichiometric or alumina-rich spinel due to their better sintering with magnesia.[25] Both in situ spinel and Mg-rich spinel were expected to increase bonding of coarse and medium particles with fine powder in the brick during sintering which would reduce porosity and increase HMOR, increasing resistance to erosion at high temperature during operation of the RH degasser in the steel plant. Table 1 shows vendor-provided (per test certificate) chemical composition and density data of the raw materials. Like DBMC bricks, 50 wt% each of spinel (14% in situ and 36% sintered) and periclase (25 wt% each of fused MgO and sintered MgO) were maintained as shown in Table 2. This would make the brick compatible with low basicity RH degasser slag ($CaO:SiO_2$ weight ratio of 1.5-2) and optimize thermal shock resistance through microcrack formation due to thermal expansion coefficient mismatch between spinel (8.4×10^{-6} K^{-1}) and periclase (13.5×10^{-6} K^{-1}).[26,28] The average particle size d_{50} values provided (obtained from laser diffraction or sedimentation methods) are from supplier data sheets and d_{SEM} is the average grain size obtained from around 700 grains in SEM images of pressed pellets. (Z, S, P) indicate the phase (cubic ZrO_2, spinel or periclase respectively) expected to evolve from that raw material during sintering. The third row has both S and P because 4% of the MgO will be consumed to form in situ spinel.

Suruga et al[34] compared magnesia-spinel bricks containing industrial fused MgO of 200, 400, 1500, and 3000 μm grain size, and concluded that corrosion resistance plateaued with a 400 μm grain size. Thermal shock resistance of bricks containing industrial sintered magnesia of 80 μm grain size was better because the smaller grain size led to a reduction in thermal expansion compared to fused MgO of larger grain size. Hence in the composition SP, 25 wt% of Chinese 97% pure fused magnesia (500 μm grain size) of coarse particle size (2.8-1 mm, agglomerates made up of 500 μm grains) with a high corrosion resistance was combined with 29 wt% sintered magnesia (80 μm grain size) of various agglomerate sizes having a high thermal shock resistance. Like sintered magnesia, sintered spinel (20 μm grain size) was also added in various particle sizes to optimize the thermal shock resistance. The in situ spinel and 22 μm (d_{50}) sintered spinel powder, because of its smaller size, is expected to enhance corrosion resistance by readily reacting with slag thereby increasing its viscosity locally (T_m of spinel is 2105°C).[26,35]

To enhance HMOR,[27] thermal shock resistance,[28,29] and corrosion resistance,[30,31] 2.5, 5, 7.5, 10, and 15 wt% (Z2.5, Z5, Z7.5, Z10, and Z15 in Table 2) fused monoclinic ZrO_2 (CUMI SHARP; d_{50} is 6.1 μm) was added into SP while maintaining the 1:1 weight proportion of spinel and periclase. The added monoclinic ZrO_2 may get stabilized into the cubic structure by the MgO raw material or CaO impurity during sintering[36-39] which may enhance the thermal shock resistance due to thermal expansion mismatch.[28,29] ZrO_2 addition enhances corrosion resistance due to interaction with slag forming high-melting Ca-Zr oxides[30,31] and increases HMOR by reducing the intergranular glassy phase.[27]

2.2 | Ceramic processing

To achieve the best packing efficiency, tapped densities of different combinations of coarse particles (2.8-1 mm), medium particles (1-0.1 mm), and fine powder (<90 μm) were evaluated. The theoretical density of each composition was calculated using the bulk density of each raw material (Table 1) taking the corresponding volume fractions into account. The combination of coarse:medium:fine 40:25:35 weight ratio (40.3:25.4:34.3 volume ratio) was selected for the composition SP. The fine powder portion, known as the matrix of a refractory, affects its field performance significantly. The tapped density of SP through Z15 is expected to be around 80% because the tapped density of a mixture of sintered spinel (AR90; Almatis Alumina Pvt Ltd; 3.40 g/cm^3 density), MR66 sintered spinel, and fused monoclinic ZrO_2 (41:30:29 volume ratio) was 80%. To ensure homogeneity of

TABLE 1 Vendor-provided chemical composition (wt%) and density of raw materials

	MgO	Al_2O_3	CaO	SiO_2	Fe_2O_3	$ZrO_2 + HfO_2$	$Na_2O + K_2O$	Density (g/cm^3)
Fused MgO	97.15	0.20	1.40	0.65	0.60	0.00	0.00	3.50
Sintered MgO	98.10	0.10	1.35	0.35	0.10	0.00	0.00	3.45
Sintered $MgAl_2O_4$	33.00	66.29	0.39	0.09	0.20	0.00	0.03	3.30
Calcined Al_2O_3	0.00	99.60	0.00	0.02	0.02	0.00	0.30	3.92
Monoclinic ZrO_2	0.04	0.12	0.09	0.28	0.05	99.17	0.00	5.60

Raw material	Particle size[a]	Wt% composition of refractories					
		SP	Z2.5	Z5	Z7.5	Z10	Z15
Monoclinic ZrO_2 (Z)	d_{50} = 6.1 μm	0	2.5	5	7.5	10	15
Sintered $MgAl_2O_4$ (S)	d_{50} = 22 μm	12.5	11.25	10	8.75	7.5	5
Sintered MgO (S, P)	d_{SEM} = 3.0 μm	12.5	11.25	10	8.75	7.5	5
Calcined Al_2O_3 (S)	d_{50} = 4.7 μm	10	10	10	10	10	10
Sintered $MgAl_2O_4$ (S)	(1-0.1 mm)	8.5	8.5	8.5	8.5	8.5	8.5
Sintered MgO (P)	(1-0.1 mm)	16.5	16.5	16.5	16.5	16.5	16.5
Sintered $MgAl_2O_4$ (S)	(2.8-1 mm)	15	15	15	15	15	15
Sintered MgO (P)	(2.8-1 mm)	0	0.63	1.25	1.88	2.5	3.75
Fused MgO (P)	(2.8-1 mm)	25	24.38	23.75	23.13	22.5	21.25

[a]In the refractory literature, particles are often referred to as grains, and grains inside coarse particles are often referred to as crystallites to emphasize on the impact of crystallite size on corrosion behavior.

TABLE 2 Targeted composition of fabricated refractories in wt%. SP is spinel-periclase refractory, whereas Z2.5 to Z15 are spinel-periclase refractories containing ZrO_2 in respective wt%

the ZrO_2 additive and in situ spinel, fine powder (<90 μm) was first mixed. Hand mixing was used because each batch size was too small for a mechanized mixer. Similarly, the coarse particles and medium particles were each separately mixed. 3 wt% dextrin was used as green binder and 2 wt% water was added to achieve workability. The mixing was done in steps to ensure a homogeneous coating of the matrix on the coarse and medium particles. First, the coarse particles were mixed with half of the water and dextrin. Then 70% of the fine particles was subsequently added to it, followed by the medium particles. Finally, the remaining water, dextrin, and fine particles were added and mixed together. Rectangular bars (150 mm x 26.7 mm x 25.5 mm) and cylinders (diameter 50.5 mm and height 58.8 mm) were uniaxially pressed at 200 MPa in a hydraulic press. To reduce the density gradient owing to die wall friction during pressing which can later cause deformation of bars during sintering, bars were first pressed at 80 MPa without dwell in a floating die, then spacer of bottom punch was removed and finally pressed at 200 MPa for 1 minute. This was done to mimic double-action uniaxial pressing of refractory bricks in the industry. After drying at 150°C for 24 hours, samples were fired in a box furnace per the schedule shown in Figure 2. The dwell time of 1 hour at 330°C was given to decompose $Mg(OH)_2$ which may form from reaction of sintered magnesia with the water added during mixing.[40,41] The slow heating rate up to 500°C was imposed to burnout the binder, whereas the dwell time for 0.5 hours at 1300°C was set to nucleate spinel.[33] For sintering, a dwell time of 2 hours at 1700°C was applied. Cooling rate was reduced to 1°C/min below 1100°C to reduce stress generated due to phase transformation of any remaining unstable ZrO_2.

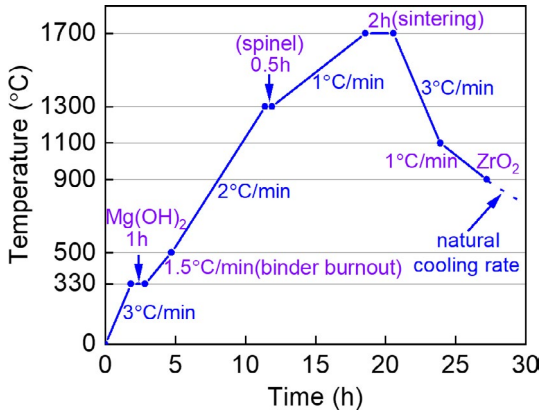

FIGURE 2 Schematic diagram of sintering schedule

2.3 | Characterization techniques

The phase composition of a ground sample prepared from the sintered refractories was analyzed using powder XRD at a scanning rate of 1°/min (Miniflex-II desktop X-ray diffractometer and SmartLab Bragg Brentano X-ray diffractometer, both from Rigaku).Quantitative phase analysis via Rietveld refinement was done using JADE 7 (Material Data

Incorporated). Microstructure of polished sections of the sintered refractory was analyzed using SEM-EDS (SU6600 FESEM; Hitachi equipped with EMAX X-act EDS; Horiba). Bulk density and apparent porosity (open porosity) of the sintered bar samples were measured using Archimedes' technique through vacuum impregnation of kerosene (ASTM standard C830-00).[42] Average (volumetric median) pore diameter was measured on a cut and polished 20 mm cube specimen using mercury intrusion porosimetry (Autopore IV; Micromeritics). Compressive strength, commonly referred to as cold crushing strength (CCS) in case of refractories was measured on cylindrical samples using a compressive strength testing machine (Chemisches Laboratorium für Tonindustrie, as per ASTM standard C133-97).[43]Flexural strength, commonly termed MOR of bar samples was measured (NETZSCH 422) at ambient temperature (CMOR) and at 1500°C (HMOR). Thermal shock resistance was quantified by measuring the percentage reduction in MOR after five cycles of quenching from 1300°C to ambient temperature in air (15 minutes dwell time at each step, based on ASTM standard C1171-05).[44]

A static slag cup test was done to analyze corrosion resistance. RH degasser slag was collected from a major Indian steel plant producing high carbon manganese steel for railway applications, where issues of the slag sticking on the exterior snorkel and removed by a deskulling machine were prevalent. These chunks of slag contained metal. The metal pieces were removed manually during crushing. Wet chemistry techniques[45] were used to analyze chemical composition of the slag(CaO-30.9%, MgO-9.8%, SiO_2-16.7%, Al_2O_3-1.4%, Fe_2O_3-37.8%, MnO_2-2.9%, TiO_2-0.5%) and its basicity was calculated (CaO:SiO_2 weight ratio is 1.9). The refractory cup was made by drilling a cavity of 10 mm diameter and 20 mm depth into arefractory cylinder of 50 mm diameter and 58 mm height. RH degasser slag powder was poured into the cup which was heated in a box furnace at 1°C/min to1650°C, held for 3 hours and cooled at 3°C/min to 900°C. A cross-section of the cup was prepared and penetration of the black-colored slag into the yellow-colored refractory was measured using a digital caliper (accuracy of 0.03 mm). Microstructure of polished specimens of the slag-refractory reaction interface were studied using SEM-EDS (Tescan GAIA3 equipped with X-Max Aztec EDS; Oxford instruments). This EDS has150 mm^2 silicon drift detector producing very high signal to noise ratio which enabled study of interparticle regions in pristine samples and cracks in thermally shocked specimens. The experimental results were compared with thermodynamic calculations performed with FactSage thermochemical software version 7.3 using the Equilib and phase diagram modules and the commercial databases FactPS and FToxid.[46] Equilibrium calculations were performed to evaluate the chemical stability of the refractory using its overall composition given the proportion and composition of each raw material. The chemical reactions between slag and refractory were simulated by the relative addition of refractory (x, in mass) to the slag ($1 - x$, in mass).

3 | RESULTS

3.1 | Phase and microstructure evolution

In order to facilitate 14 wt% in situ spinel formation during sintering, 10% alumina powder was added to the composition SP. Hence corundum (ICDD PDF# 00-046-1212) is seen in the XRD pattern (Figure 3) of unsintered SP. Complete in situ spinel formation in SP sintered at 1700°C is confirmed by the XRD pattern. Phase quantification shows that after sintering the refractory contained nearly 50% of spinel (ICDD PDF# 00-021-1152) and periclase (ICDD PDF# 00-045-0946) respectively. Along with spinel and periclase, complete stabilization of added monoclinic ZrO_2 into the cubic polymorph (ICDD PDF# 00-049-1642) was seen in Z2.5and Z15. The MgO-Al_2O_3-ZrO_2 ternary phase diagram[36] predicts that compositions Z2.5 to Z15 above 1600°C form cubic ZrO_2, spinel, magnesia, and a metastable ternary phase X ($Mg_{5+x}Al_{2.4-x}Zr_{1.7+0.25x}O_{12}$ where $-0.4 \leq x \leq 0.4$). X decomposes below 1600°C and the final stable phases are spinel, periclase, and cubic ZrO_2.

Additionally, SEM-EDS analysis of ZrO_2particles show that the Mg/Ca ratio increases from Z2.5 (1.09) through Z10 (1.35) to Z15 (1.74), Table S1. According to phase equilibrium calculations performed with FactSage for Z2.5 and Z15, the Mg/Ca ratio in cubic ZrO_2 in Z15 above 1467°C (Figure 4) is much larger than Z2.5.With increasing temperature, the solubility of Mg increased rapidly in both

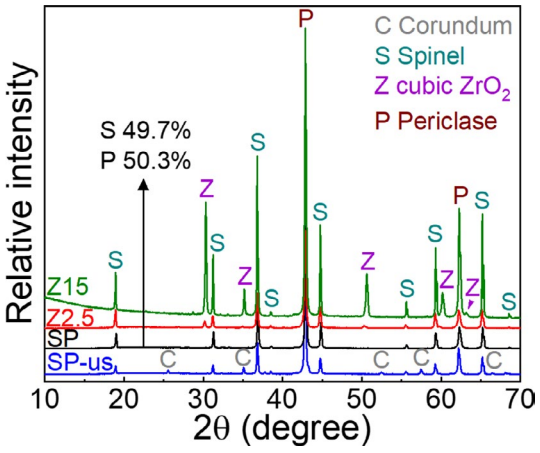

FIGURE 3 Powder X-ray diffraction pattern showing presence of corundum in unsintered SP (SP-us) which reacted completely during sintering at 1700℃ for 2 h to form in situ spinel (SP, Z2.5, Z15). Cubic ZrO_2 is seen in both Z2.5 and Z15. Inset values show 1:1 weight ratio of spinel and periclase in SP after sintering

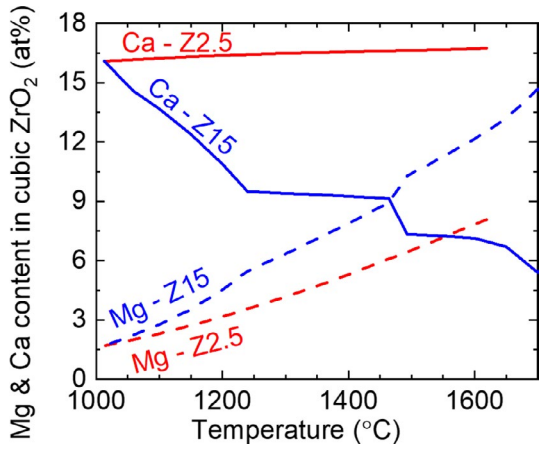

FIGURE 4 Calculated temperature dependent Mg and Ca content at equilibrium in cubic ZrO_2 phase in compositions Z2.5 and Z15

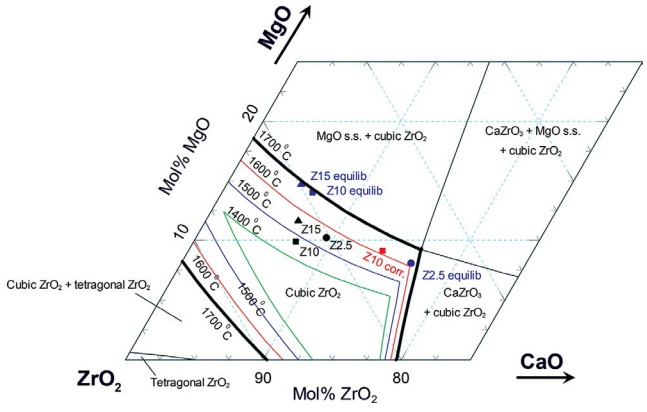

FIGURE 5 Calculated phase diagram of the ZrO_2-rich corner of the CaO-MgO-ZrO_2 system along with boundaries of the cubic ZrO_2 solid solution at different temperatures. The blue, black, and red markers represent the compositions of the cubic ZrO_2 phase from equilibrium calculations, and energy dispersive spectroscopy analysis of pristine as well as slag-corroded samples respectively

Z2.5 and Z15. At equilibrium, the cubic ZrO_2 phase in Z10 and Z15 at 1700°C is saturated with MgO as shown by the blue markers on the boundary line between cubic ZrO_2 and MgO+ cubic ZrO_2 phase fields in Figure 5. However, EDS analysis showed that the Ca and Mg content in the cubic ZrO_2 is lower than the equilibrium values, as represented by the black markers in Figure 5. These three markers are located inside the single phase cubic ZrO_2 stable region for temperatures above ~1550°C. Given that the sintering temperature is 1700°C, the phase diagram, therefore, indicates that the measured ZrO_2 cubic phases are stable. The CaO-ZrO_2[38] and MgO-ZrO_2[39] phase diagrams show the solubility limit of CaO and MgO in cubic ZrO_2 at 1700°C is 18.9 and 18.6 mol% respectively. However, when present simultaneously, the FactSage ternary CaO-MgO-ZrO_2 phase diagram shows that the maximum solubility in cubic ZrO_2 at 1700°C is 16.8 mol% CaO and 9.2 mol% MgO (upper-right corner of bold black line in Figure 5), which sum up to 26 mol%.

The SP composition has a dense microstructure where coarse spinel and periclase particles are embedded in a homogeneous matrix of a mixture of fine particles of spinel and periclase, Figure 6A. A similar dense microstructure is seen in Z10 (Figure 6B) where the matrix (evolved from <90 μm powder) contains a homogenous distribution of cubic ZrO_2 particles (white) along with fine spinel and periclase. The homogeneous distribution of ZrO_2 and the absence of its agglomerates is highly desired in the microstructure. ZrO_2 can have a beneficial effect on high temperature strength of the refractory which will be discussed later. Z10 was selected for analysis because the failure mechanisms were magnified in this composition and hence it will help in comparison.

Closer inspection of the cubic ZrO_2 particles in Z10 revealed that most (77% out of 13 inspected) are crack-free (Figure 7A), while a few (23%) have multiple cracks (Figure 7B). These cracks which formed despite a slow cooling rate of 1-3°C/min during sintering, could be attributed to the decomposition of the ternary phase X ($Mg_{5+x}Al_{2.4-x}Zr_{1.7+0.25x}O_{12}$ where $-0.4 \leq x \leq 0.4$) which involves a 10% volume change which can create severe strain in the refractory.[36]

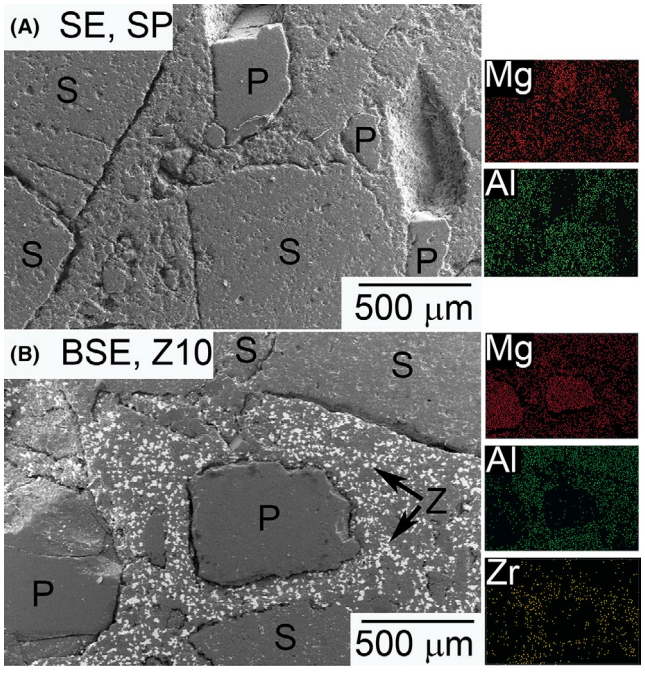

FIGURE 6 A, Secondary electron image of the SP microstructure showing coarse spinel (S) and periclase (P) particles. B, Back scattered electron micrograph of Z10 showing fine white ZrO_2 (Z) particles in the matrix

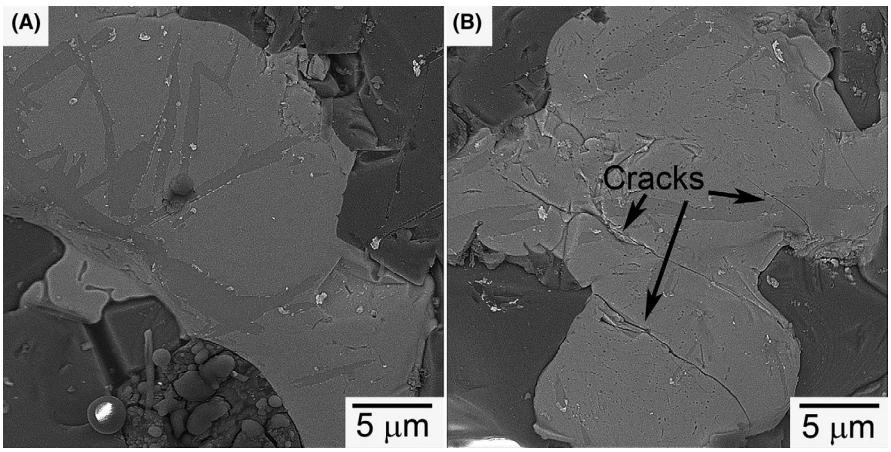

FIGURE 7 Secondary electron images of ZrO_2particles(light colored) in Z10: (A) uncracked and (B) cracked

3.2 | Densification

Despite the fact that spinel formation results in 7.4% volume expansion,[26,47] the composition SP containing 14 wt% in situ spinel exhibited 0.8% firing shrinkage (Table 3) and a low apparent porosity of 12.7% (Figure 8). The reported value of apparent porosity of DBMC bricks is 11%-18%,[15,23] and that of spinel-containing chrome-free bricks is 13%-16%.[10,15] The low porosity in SP is because it has high tapped density as explained in Section 2.2.The high tapped density and double-action uniaxial pressing led to green densities in the range 87%-90% (Figure 8). Hence, sintering did not cause any densification (reduction of porosity), but did lead to bonding of coarse and medium particles with the matrix. Addition of ZrO_2slightly increases the bulk density because ZrO_2 is denser than spinel and MgO. The apparent porosity first slightly reduces, then increases with further ZrO_2 addition and reaches 13.4% in the case of Z15. The average pore diameter of SP is 9.87 μm (Table 3) which is lower than the reported values of DBMC bricks (18-23 μm) and chrome-free spinel-containing bricks (10-80 μm).[10,48] With the addition of ZrO_2 to SP, the pore size increases to a maximum of 19.65 μm in Z7.5 and reduces to 12.6 μm in Z15.

3.3 | Strength at ambient and high temperature

Reasonably good CCS is preferred for refractory bricks as it may help in reducing damages during handling. The CCS of SP composition was 51 MPa (Figure 9) which is close to the lower range of DBMC bricks for the RH degasser (54-142 MPa, dashed blue vertical double-sided arrow),[10,11,22,23]but better than spinel-containing chromium-free refractories (21-39 MPa).[10]The error bars for the CCS values are equal because they represent the overall average standard deviation for different spinel-containing refractories, some of which will be published later, where each composition had three specimens. Contrary with the popular behavior observed in ceramics,[49] in case of the studied compositions, CCS is having a direct relationship with porosity of the material as evident from Figures 8 and 9. The decrease in CCS due to ZrO_2 addition seems to be related to an overall reduction in liquid phase assisted sintering (Figure 10).

Higher HMOR (flexural strength) implies higher resistance of the refractory to erosion[12,14] by turbulent circulation of molten steel and slag which is even more severe in the inlet snorkel due to argon gas bubbles (Figure 1). The HMOR of SP is 3.6 MPa at 1500°C, which is near the lower limit of DBMC bricks (4-9 MPa, solid red vertical double-sided arrows in Figure 9)[12,14,15] and like that of spinel-based chromium-free refractories used in the RH Degasser (2-6 MPa).[10,15] The high strength indicates good bonding due to in situ spinel formation and a low-impurity matrix. The compositions with ZrO_2 show increase in HMOR which nearly doubled in case of Z15. To investigate the microstructural and chemical origin of increased HMOR in zirconia-bearing compositions relative to SP, and to investigate their implications on erosion resistance, SEM-EDS analyses were performed at interparticle regions. Figure 11A shows SEM-EDS line scans along three spinel particles in SP. Increased

TABLE 3 Effect of ZrO_2 addition on firing shrinkage and average pore diameter of spinel-periclase compositions

	SP	Z2.5	Z5	Z7.5	Z10	Z15
Shrinkage (%)	0.82	1.13	1.14	1.0	0.93	1.04
Average pore diameter (μm)	9.87	16.95	16.94	19.65	16.98	12.6

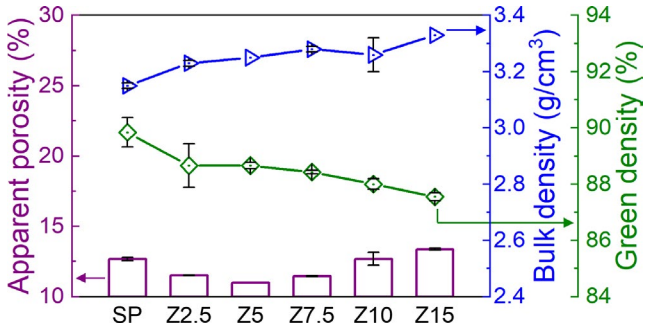

FIGURE 8 Effect of ZrO_2 addition on apparent porosity, bulk density, and green density of spinel-periclase compositions

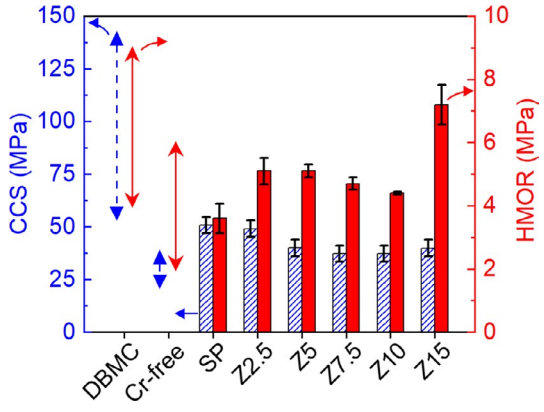

FIGURE 9 Impact of ZrO_2 addition on cold crushing strength and hot modulus of rupture at 1500℃ of spinel-periclase compositions

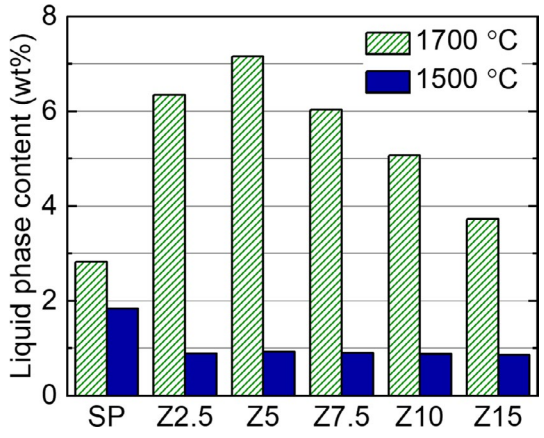

FIGURE 10 Calculated liquid phase content at equilibrium in the compositions at 1700℃ and 1500℃, which influence sintering and hot modulus of rupture respectively

amount of Si is present in the first interparticle region between the two spinel particles and the second spinel-spinel interparticle region is thicker (~2 μm) and is rich in both Si and Ca. Figure 11B shows EDS line scan along three interfaces: spinel-periclase, periclase-periclase, and periclase-spinel. The second periclase-spinel interparticle region has an accumulation of Si and Ca. In the Z15 composition, cubic ZrO_2particles (marked Z) take Ca and Fe into solid solution according to the SEM-EDS line scans (Figure 12). In contrast with the SP refractory (Figure 11A), spinel-spinel (S-S) interparticle regions in Z15 do not show any Ca and Si enrichment. Some Si and Ca enrichment (marked by black dotted box) is seen near the spinel-periclase (S-P) interparticle region in Z15.

3.4 | Thermal shock resistance

Although HMOR increased with ZrO_2 content, thermal shock resistance of the spinel-periclase compositions deteriorated with ZrO_2 addition (Figure 13). The MOR (ie flexural strength) decreased by a smaller percentage in SP than in Z15, indicating that SP has better thermal shock resistance. Flexural strength loss of SP was only 68%, whereas the ZrO_2-containing compositions showed strength loss between 82%-87%. Retained strength of SP was 5.9 MPa, double that of Z15 (2.8 MPa). This is contrary with reports by Ceylantekin and Aksel[28] who reported an improvement of thermal shock resistance in magnesia-spinel composites due to ZrO_2 addition, though their composites were made of different raw materials and did not contain coarse particles (2.8-1 mm) which constitutes 40 wt% of our compositions.

Periclase particles with a higher thermal expansion coefficient (13.5×10^{-6} K^{-1}) than the surrounding spinel phase (8.4×10^{-6} K^{-1})[26] were seen to be detached from the matrix creating fracture porosity around them in SP (Figure 14). Such voids, usually termed incorrectly as 'fractal pores' in refractory literature,[25] are common in magnesia-spinel refractories and are known to increase thermal shock resistance. Thermal shock resistance, R′, is given by the heat flux parameter, Equation (1),

$$R' = \frac{\sigma_f(1-\nu)\kappa}{E\alpha}, \quad (1)$$

where σ_f is the fracture strength (eg MOR),ν is the Poisson's ratio, κ the thermal conductivity, E the elastic modulus, and α is the coefficient of thermal expansion.[50] Cubic ZrO_2 has a high thermal expansion coefficient (~10.5×10^{-6} K^{-1}) and low thermal conductivity (~2 W/mK).[50] Hence, theoretically ZrO_2 addition should reduce thermal shock resistance of the spinel-periclase compositions. Fracture porosity, which improved thermal shock resistance of SP composition was not observed in Z10 (Figure S1) which could be because the mismatch in thermal expansion between the large MgO particles and the matrix reduces due to ZrO_2 addition. The thermal shock is believed to generate differential thermal stress between ZrO_2-rich

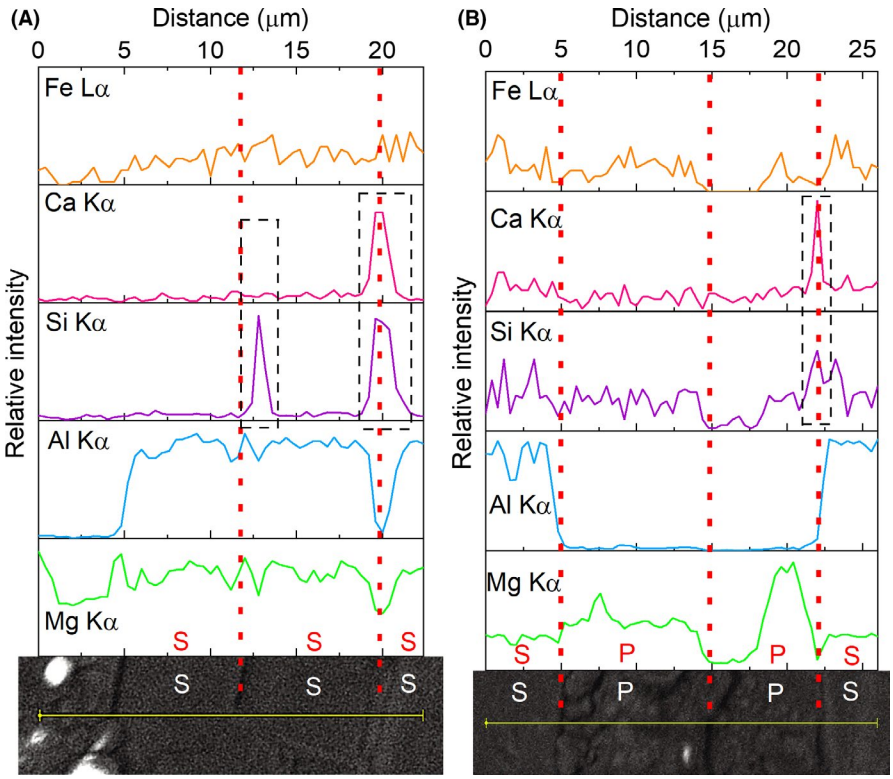

FIGURE 11 Scanning electron microscopy coupled with energy dispersive spectroscopy line scans in the composition SP showing Ca and Si rich interparticle regions between (A) spinel-spinel and (B) periclase-spinel particles indicated by black dotted boxes. S and P indicate spinel and periclase particles. Vertical red dotted lines indicate interfaces

regions and surrounding ZrO_2-deficient regions. A 500 μm long and up to 30 μm wide thermal shock induced crack is seen to propagate along the interface between a ZrO_2-rich and ZrO_2-deficient region in Figure 15A. Bright particles are cubic ZrO_2. EDS maps in Figure 15B clearly show that MgO and spinel are evenly distributed on both sides of the crack, but ZrO_2 particles are only observed on the lower side. An SEM image (Figure 16) of a cubic ZrO_2 particle in thermal shocked Z10 having small cracks looks like that before thermal shock (Figure 7B). The proportion of cracked ZrO_2 particles in Z10 after thermal shock (23.5% among 17 particles analyzed) is the same as before thermal shock (23% among 13 particles).

3.5 | Slag corrosion resistance

The RH slag collected from the steel plant is expected to be rich in FeO due to the vacuum environment and slag contact with molten steel at high temperature. However, the slag corrosion tests were performed at 1650°C in air without molten steel. Under these conditions, FactSage equilibrium calculations predicted this slag to be liquid (T_m was 1497°C) with a composition (in wt%) of: Fe_2O_3 31.9, FeO 5.6, CaO 31.2, SiO_2 16.9, MgO 9.9, Al_2O_3 1.4, Mn_2O_3 1.7, MnO 0.9, and TiO_2 0.5. There are three main corrosive oxides in the slag:FeO_x, CaO, and SiO_2. Base composition SP showed the least penetration (2.6 mm) by molten RH degasser slag (Figure 17) meaning SP has a higher corrosion resistance. One measurement each was made for both penetration depth as well as pore diameter. Slag penetration increased with ZrO_2 addition reaching a maximum for Z10 (7.1 mm), after which it reduced slightly in Z15 (4.9 mm). Hence, Z15 has better corrosion resistance among the ZrO_2-containing compositions.

Figure 18 shows an SE image and EDS maps of a representative portion of composition SP with spinel and MgO particles of various sizes that were in contact with RH degasser slag. Considering the tendency for continuous and uniform infiltration starting from the slag region, Fe is found to be more aggressive, apparent by a thick and uniform region of high Fe concentration, followed by a thin layer of Ca and more subtle penetration of Si. With increasing distance from the slag contact area (going downwards), FeO_x penetration decreases possibly because the connectivity of open pores is gradually lost. The relative resistance of sintered MgO, fused MgO and spinel toward FeO_x penetration is clarified by the next two figures.

A large fused MgO particle in slag corroded SP is shown in Figure 19. It is easily identified by (a) its dense and somewhat elevated appearance because the surrounding porous regions get polished down more during SEM sample preparation (hardness decreases exponentially with increasing porosity[51]); and (b) the fact that MgO particles larger than 1 mm in SP can only consist of fused MgO (Table 2). Figure 19 additionally corroborates the slag corrosion behavior of SP observed in Figure 18. The dense fused MgO particle in Figure 19 is seen to be devoid of Fe. The line averaged Fe scan performed using Gatan Digital Micrograph software (GMS3; Gatan) over a

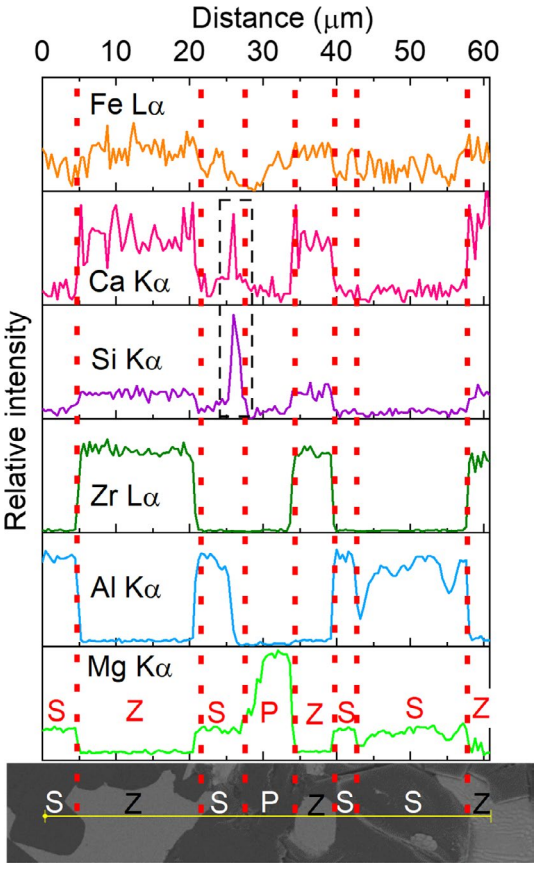

FIGURE 12 Scanning electron microscopy coupled with energy dispersive spectroscopy line scans in the composition Z15 show only a Ca and Si enrichment at the spinel-periclase (S-P) interparticle region which can form low-melting phases. Vertical red dotted lines indicate interfaces

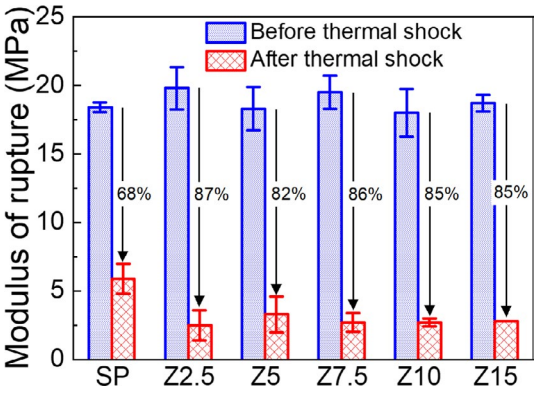

FIGURE 13 Impact of ZrO_2 addition on thermal shock resistance of spinel-periclase compositions. Percentage reduction in modulus of rupture of refractory bars after five cycles of quenching from 1300°C to ambient temperature air is shown

rectangular region illustrates that the Fe concentration abruptly decreases in the fused MgO particle.

Figure 20 shows the calculated refractory stability and equilibrium composition of the slag in contact with SP at

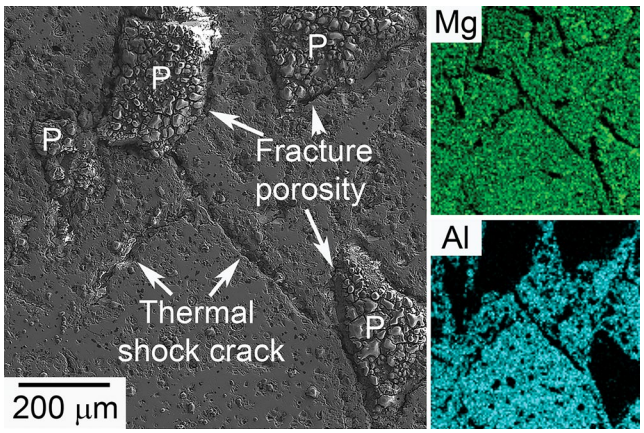

FIGURE 14 Secondary electron image and energy dispersive spectroscopy maps of spinel-periclase composition after five cycles of thermal shock from 1300°C to ambient temperature air. Thermal shock induced cracks are seen to be stopped at fracture porosity formed around periclase (P) particles

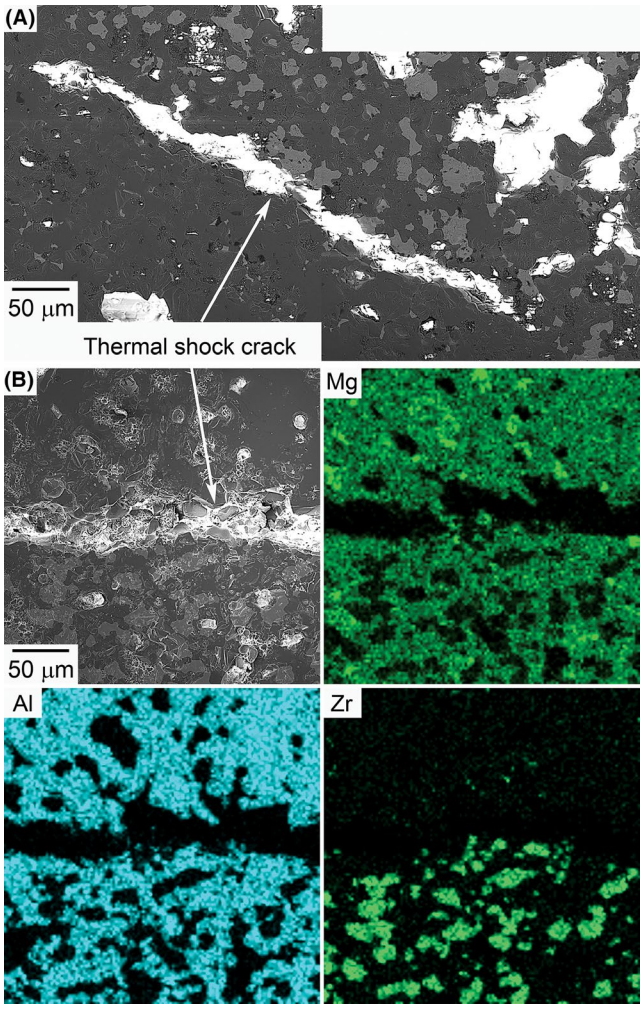

FIGURE 15 A, Secondary electron image of a 500 μm long thermal shock induced crack in Z10. Another similar crack (B) is shown with energy dispersive spectroscopy maps clarifying the crack propagates at the interface between ZrO_2-rich and ZrO_2-deficient region

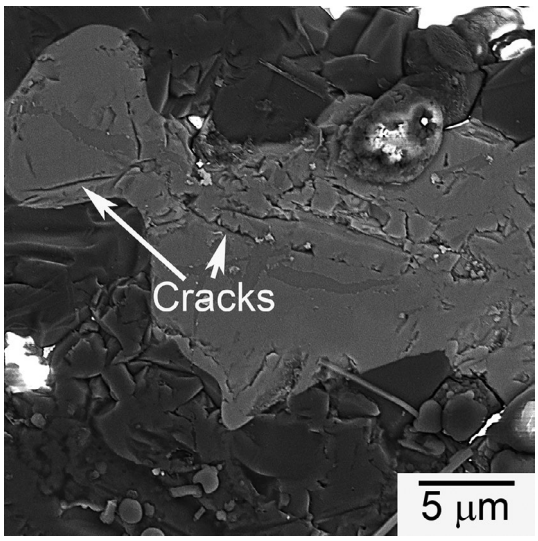

FIGURE 16 Secondary electron image of a ZrO_2 particle (light colored) in Z10 after thermal shock showing small cracks

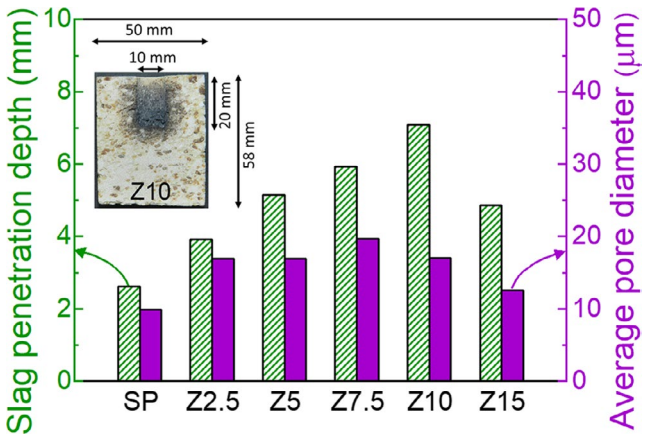

FIGURE 17 Impact of ZrO_2 addition on depth of penetration of Ruhrstahl Heraeus degasser slag into spinel-periclase refractories reacted at 1650℃ for 3 h. Diameter of pores in the refractories are seen to have a strong influence. Inset shows cross-section of the refractory cup of Z10 composition after slag corrosion

1650°C. According to these calculations which assume perfect contact and instant reactions between all phases, the spinel phase from SP is less stable in the RH slag than the MgO phase, as evident by the lower spinel phase content at a given SP mass fraction, and by the presence of MgO close to the slag-rich side (Figure 20A). This is because the slag has a higher solubility of Al_2O_3 (36 wt%) than MgO (18 wt%), Figure 20B. However, dissolution of spinel in the slag could not be observed in the SEM images, possibly because the slag-rich regions were partially lost during SEM polishing. The measured Fe content in spinel and MgO particles were higher than the FactSage predictions (Table S2).

Figure 21 shows microstructure of Z10 where slag is penetrating downwards. The elemental maps show a large fused MgO particle on the right (P), a small fused MgO particle in the bottom left and a matrix of ZrO_2, MgO as well as spinel in the middle. The fused MgO particles were identified by their dense and slightly elevated appearance. White line scan 1 shows Fe steadily penetrates the matrix containing corrosion resistant phase ZrO_2, and it is inhibited only when it faces the fused MgO particle. White line scan 2 shows Fe extensively reacts into the first 250 μm of the large fused MgO particle and then gets strongly inhibited. However, as soon as it enters the matrix, the Fe concentration becomes as high as in the slag contact region.

Figure 22 shows the interaction of RH degasser slag with the ZrO_2-infused matrix in Z10. Point EDS analysis in Table 4 reveals that cubic ZrO_2 particles interacted with CaO from the infiltrating slag (a) by forming $CaZrO_3$ phase; and (b) by increasing the Ca content in the solid solution in cubic ZrO_2 particles from 7.0 ± 0.6 at% in pristine Z10 (Table S1) to 13.0 ± 1.4 at% in slag corroded Z10. The (Ca + Mg)/(Ca + Mg+Zr) ratio in Z10 after slag corrosion was 0.23 which is in accordance with the FactSage prediction of 0.25 at 1650°C .

Figure 23A-C presents the thermodynamic predictions of the chemical interactions between Z10 and the RH slag. The simulations reveal that MgO resists corrosion, while both spinel and cubic ZrO_2 dissolve in RH slag, Figure 23A, due to the high solubility of Al_2O_3 and ZrO_2in the slag. As a result, the slag splits into two immiscible liquids, so-called "slag 1",which can dissolve up to 20 wt% Al_2O_3 and 15 wt% ZrO_2, Figure 23B, and ZrO_2-rich slag 2, which can dissolve up to 29 wt% Al_2O_3 and 35 wt% ZrO_2, Figure 23C. The viscosity of slag 1 was found to increase as it infiltrated Z10. Viscosity of slag 2 could not be calculated with FactSage due to the high ZrO_2 content.

4 | DISCUSSION

Chromium-bearing DBMC refractories are the current standard for the RH Degasser lower vessel and snorkel linings. Being a potential source of carcinogenic Cr^{6+}, an alternative chromium-free refractory meeting the stringent properties requirements is the need of the hour. The present study on the spinel-periclase-zirconia system brings to light the key parameters that need to be addressed to achieve the required properties in a chromium-free system. Development of the alternative chromium-free refractory was enabled by the meticulous design of materials and processing. The selected 40:25:35 weight ratio of coarse, medium, and fine particles led to very high green and sintered densities. The adopted floating die mechanism mimicking industrial double-action pressing as well as the customized sintering regime allowed

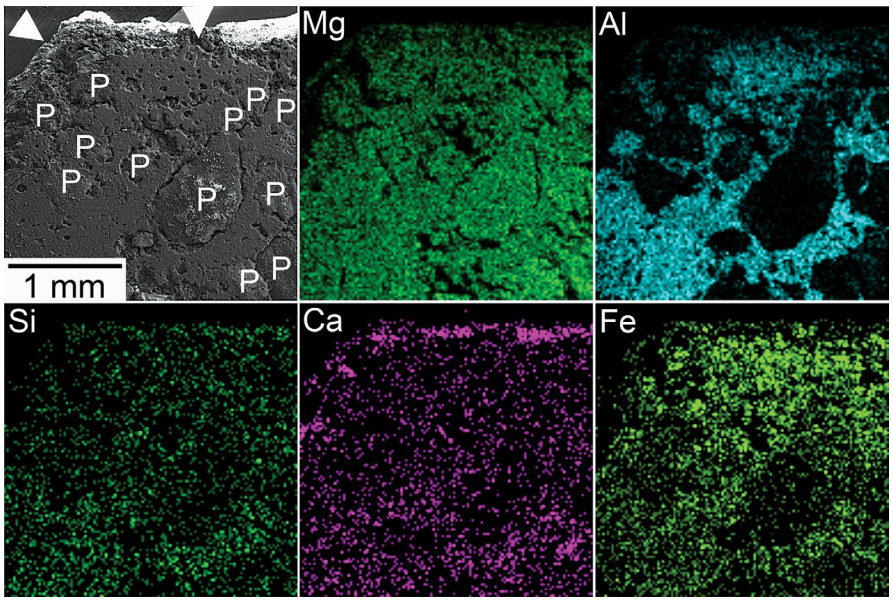

FIGURE 18 Secondary electron image of Ruhrstahl Heraeus degasser slag corroded composition SP at a region having various particle sizes of spinel and periclase. White arrowheads indicate direction of slag penetration. Mg and Al energy dispersive spectroscopy (EDS) maps in the top row identify periclase particles (P). Si, Ca, and Fe EDS maps in bottom row illustrate penetration of slag elements

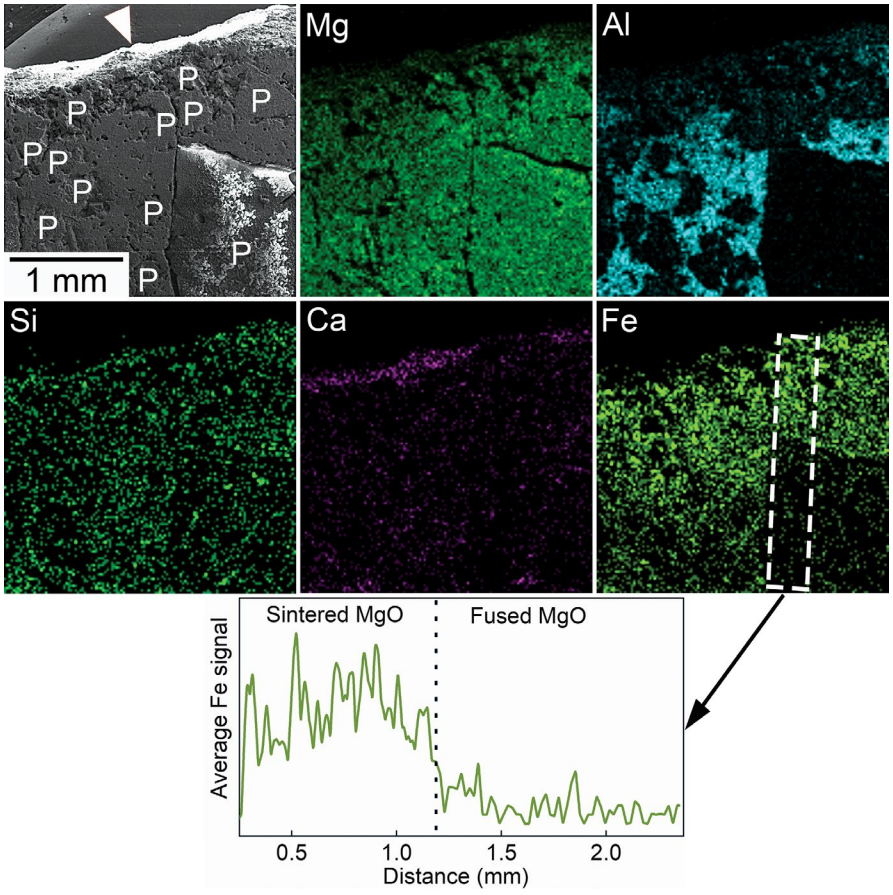

FIGURE 19 Secondary electron image of Ruhrstahl Heraeus degasser slag corroded composition SP showing a large fused MgO particle (bottom right). White arrowhead indicates direction of slag penetration. Mg and Al energy dispersive spectroscopy (EDS) maps in the top row identify periclase particles (P). Si, Ca, and Fe EDS maps in middle row illustrate penetration of slag elements. Integrated line scan along a rectangular region (dotted white box) in Fe map is shown at the bottom

slow removal of volatiles and gradual phase formation/transformation leading to defect-free sintered bodies. The matrix of SP composition contained free Al_2O_3 and sintered MgO which reacted to form in situ spinel during sintering which was believed to enhance HMOR. Coarse particles of fused MgO was added to impart a high corrosion resistance. The simultaneous presence of MgO and spinel phases, having disparate thermal expansion, led to a high thermal shock resistance. Their concomitant presence also helped in matching with the low basicity of RH slag. The magnesia-rich MR66 spinel was added because it bonds well with MgO during sintering. Finally, ZrO_2 which underwent in situ stabilization during sintering, was seen in microstructural investigation to have a positive impact on HMOR and corrosion resistance.

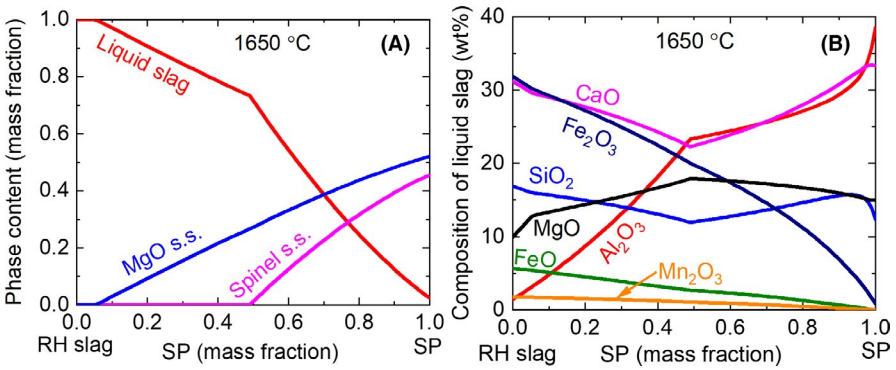

FIGURE 20 Calculated chemical stability of composition SP in equilibrium with Ruhrstahl Heraeus slag at 1650℃: (A) phase distribution showing lower stability of spinel than periclase and (B) liquid slag composition with an increasing fraction of SP

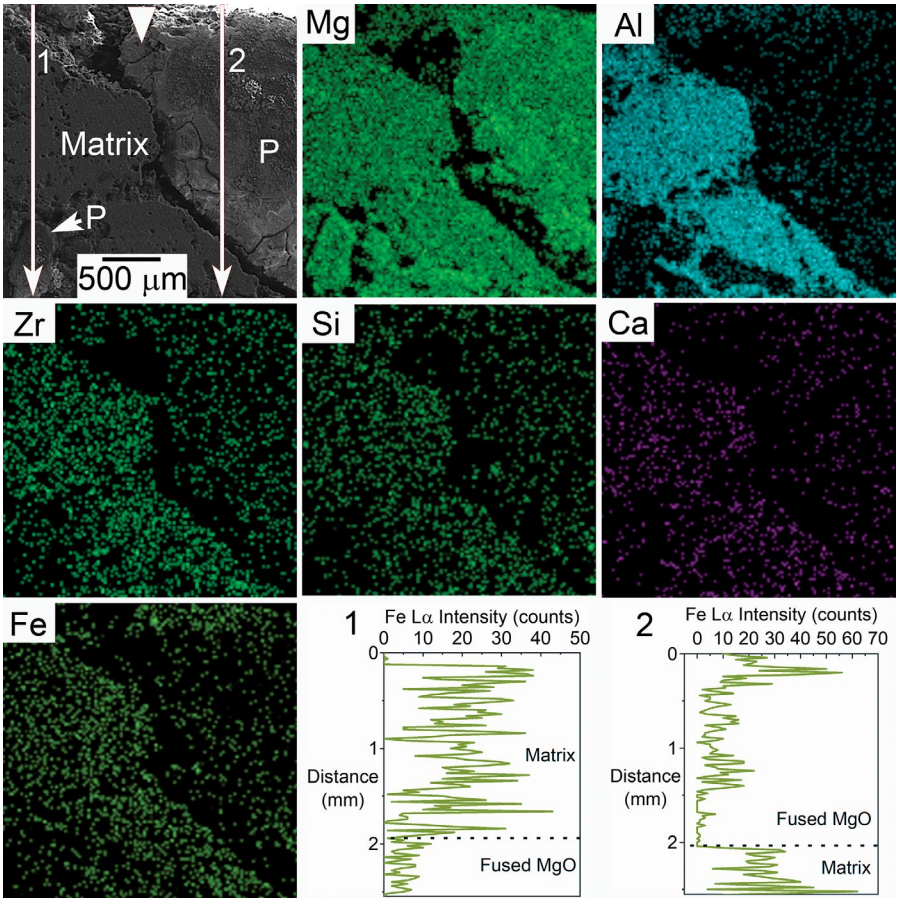

FIGURE 21 Secondary electron image of Ruhrstahl Heraeus degasser slag corroded Z10. White thick arrowhead indicates direction of slag penetration. Mg, Al, and Zr energy dispersive spectroscopy (EDS) maps identify periclase particles (P) and ZrO_2-rich matrix in the refractory. Si, Ca, and Fe EDS maps in subsequent rows illustrate penetration of slag elements. Two Fe line scans are shown: white arrow 1 passes from ZrO_2-MgO-spinel matrix into a small fused MgO particle and white arrow 2 goes from a large fused MgO particle into the matrix

The thermodynamic calculations carried out for the system as well as the slag-refractory interaction supported the experimental results.

The XRD analysis (Figure 3) showed that the sintered SP refractory composition is free from unreacted alumina, and has about 50% of spinel content, thus ensuring the effectiveness of the employed heat treatment schedule (Figure 2). A similar behavior was also observed in the case of ZrO_2-bearing compositions. Though stabilization of the monoclinic ZrO_2in cubic form was observed, no new additional phases are identified in ZrO_2-bearing compositions. A shift of the cubic ZrO_2 peaks toward higher angles is observed between Z2.5 and Z15 (2θ were 30.15° and 30.32°, respectively) indicating a decrease of lattice parameter. Duwez et al[37] reported that whereas CaO addition increases the lattice parameter of ZrO_2, MgO reduces it. This implies that, as more ZrO_2 was added to the composition SP, MgO gradually became the dominant stabilizing cation for ZrO_2 and explains the shift of the ZrO_2 XRD peaks to a higher angle in Z15. This was also confirmed by SEM-EDS analysis (Table S1). The thermodynamic calculations (Figures 4 and 5) showed higher solid solubility of CaO and MgO in ZrO_2 in combination. The simulated precipitation behavior, however, was not observed in the EDS results measured at ambient temperature possibly because of slow diffusion kinetics. The (Ca + Mg)/(Ca + Mg+Zr) ratio in the EDS results of Z2.5, Z10, and Z15 are below 0.20 which is within the solubility limit depicted in the phase diagram. It is interesting to note

that, although the MgO/CaO molar ratio in the bulk of Z2.5 and Z15 calculated from Tables 1 and 2 are 101.7 and 100.0, respectively; the Mg/Ca ratio in the cubic ZrO_2 particles are 1.09 and 1.74 respectively. This shows that ZrO_2 takes up the impurity element Ca into its structure even though Ca is present in minor quantity. This justifies the expression "lime sponge"[31] for ZrO_2 which often takes up considerable lime (CaO) into solid solution in refractories rich in spinel and MgO.[35] ZrO_2removes CaO from the interparticle regions which would otherwise react with Al_2O_3 or SiO_2 to form a eutectic interparticle glassy phase or low melting crystalline phase like monticellite ($CaMgSiO_4$, T_m is 1490°C[35]) which deteriorates high temperature strength.

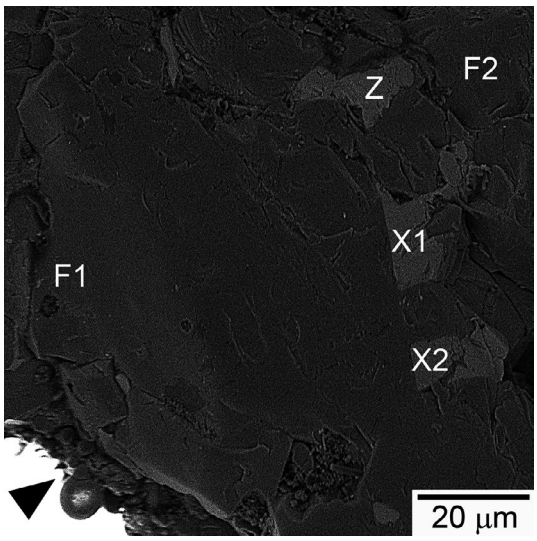

FIGURE 22 Secondary electron image of the matrix in Z10 corroded by Ruhrstahl Heraeus degasser slag. Black arrowhead indicates direction of slag penetration. Labels indicate a cubic ZrO_2particle (Z), two $CaZrO_3$particles (X1, X2), and two Fe-rich points near (F1) and away (F2) from slag

The expected expansion during in situ spinel formation was also not observed in any of the compositions (Table 3). This indicates that the expansion during spinel formation gets accommodated in the starting porosity and was compensated for by the firing shrinkage, thus confirming the effectiveness of the reported experimental design. Initially the addition of ZrO_2 in place of MgO and spinel results in slight reduction of porosity, which increases with further addition (Figure 8). From SP through Z15, increasing weight of the denser phase ZrO_2 (density 5.6 g/cm^3) replacing the lighter phases MgO and spinel (both have density~3.6 g/cm^3) reduces the powder packing density and green density, and increases the porosity due to rearrangement of the particles which is restricted by the coarse particles (2.8-1 mm). Simultaneously, the fine ZrO_2 powder (6.1 μm) is replacing an overall large-sized mixture of spinel (22 μm) and MgO (3 μm), thus reducing porosity. These two competing factors possibly lead to reduction in porosity up to Z5, followed by an increase. Additionally, the equilibrium calculations predict that the weight fraction of liquid phase at 1700°C also increases from SP to Z5 and reduces steadily through Z15 (Figure 10). Sintering is enhanced by the liquid phase, suggesting that Z5 would exhibit maximum sintering (lowest apparent porosity), which is experimentally observed (Figure 8).The pore size first increases followed by a decrease (Table 3). This is possibly due to the change in density and particle size with ZrO_2 addition. It has been commonly observed that ceramics made from smaller particles have smaller pores in pressed[52] as well as sintered bodies than ceramics prepared from larger particles.[53]Hence, to achieve a uniform low pore size

TABLE 4 Experimental and simulated compositional analysis of phases in the formulation Z10 after slag corrosion. Mean values of scanning electron microscopy coupled with energy dispersive spectroscopy (SEM-EDS) of respective particles are presented (in at %), and the given uncertainty is standard deviation. Slag saturated compositions of different refractory phases obtained through FactSage simulation is also listed here

	Spinel		MgO		Cubic ZrO_2		$CaZrO_3$	
	EDS	FactSage	EDS	FactSage	EDS	FactSage	EDS	FactSage
Spectra analyzed	4		5		17		3	
Mass fraction of Z10		0.59		0.07		0.92		
Mg	31.8 ± 1.4	33.2	87.2 ± 6.5	90.0	8.3 ± 0.6	10.7	2.8 ± 0.5	0
Al	52.4 ± 4.9	57.1	2.4 ± 1.3	0.2	2.7 ± 0.2	0.1	1.5 ± 0.3	0
Si	1.7 ± 2.8	0	0	0	0 ± 0	0	0.5 ± 0.4	0
Ca	0.5 ± 0.3	0	0.4 ± 0.9	0.1	13.0 ± 1.4	11.1	43.0 ± 6.2	50
Ti	0.1 ± 0.2	0	0.2 ± 0.3	0	0.3 ± 0.2	0	1.0 ± 0.1	0
Mn	1.0 ± 0.6	0.6	1.8 ± 1.2	0.7	0.6 ± 0.3	0	2.1 ± 0.8	0
Fe	12.5 ± 4.5	9.1	7.9 ± 4.5	9.0	4.7 ± 1.5	0.1	3.0 ± 1.5	0
Zr	0 ± 0	0	0	0.1	70.4 ± 2.8	78.0	46.1 ± 6.3	50

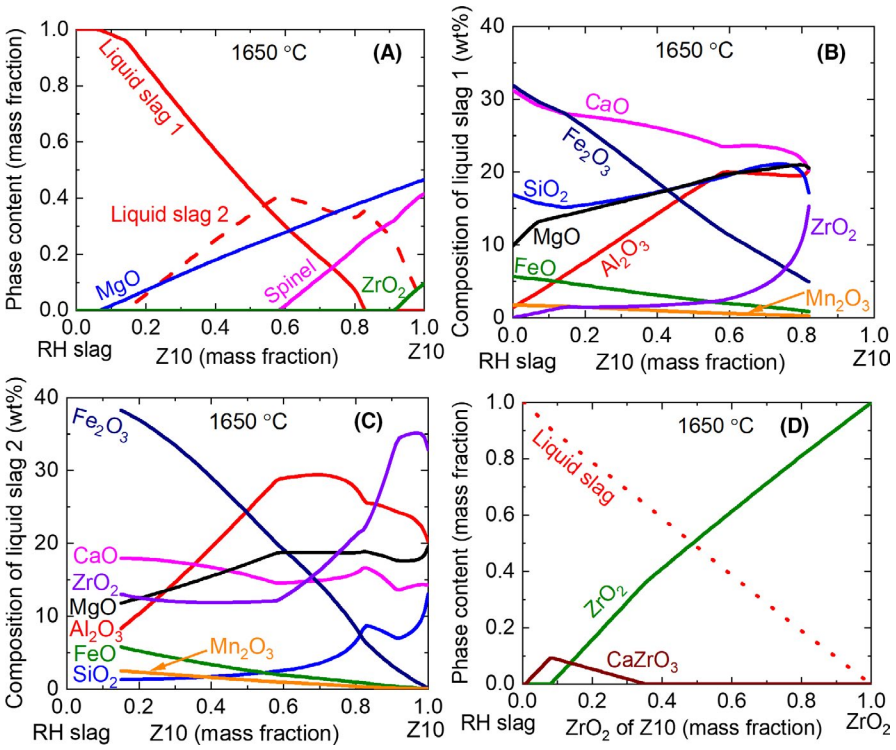

FIGURE 23 Calculated chemical stability of composition Z10 in equilibrium with Ruhrstahl Heraeus (RH) degasser slag at 1650℃: (A) phase distribution, and composition of (B) liquid slag 1 and (C) liquid slag 2 with an increasing fraction of Z10. D, Calculated phase distribution of cubic ZrO_2 in equilibrium with RH slag

distribution we can use the same particle size of fine ZrO_2, spinel and MgO powder which were in this case all different (6.1, 22 and 3 μm respectively). Additionally, the whole composition design could be based on volume instead of weight (Table 2), though the ratio of different grades of spinel and MgO that control HMOR, thermal shock resistance, and corrosion resistance, should be monitored.

The HMOR increased with 2.5% ZrO_2 addition compared to that of SP (Figure 9). Further ZrO_2 addition did not show any additional improvement until Z15 which showed a high HMOR of 7.2 MPa. This is 20% better than the best reported chromium-free spinel-containing refractory (6 MPa),[15] and approaches the upper limit of DBMC bricks. The EDS analysis of the interparticle regions in SP (Figure 11) shows presence of high Si and Ca in the interparticle regions. From the perspective of the erosion-prone environment of the RH degasser operating up to 1630°C, presence of Ca and Si at interparticle regions can prove dangerous because of formation of eutectic glass and crystalline phases including monticellite ($CaMgSiO_4$, T_m is 1490°C),[35] merwinite ($Ca_3MgSi_2O_8$, T_m is 1575°C), anorthite ($CaAl_2Si_2O_8$, T_m is 1553°C), and gehlenite ($Ca_2Al_2SiO_7$, T_m is 1593°C).[26] Liquid formation at interparticle regions would cause particles to slide under load at high temperature, reducing HMOR, and could also cause the refractory to be eroded faster under the force of rapidly moving molten steel. At the same time in case of Z15 (Figure 12), while there is a presence of Ca and Si-rich phase in spinel-periclase interparticle region, the spinel-spinel, spinel-ZrO_2, and periclase-ZrO_2 interparticle regions are clean. The overall enhancement in HMOR of spinel-periclase compositions with ZrO_2 addition could be due to removal of the CaO impurity from interparticle regions of periclase (both fused and sintered MgO contain ~1.4% CaO). Point EDS data in Table S1 shows that the cubic ZrO_2 particles in Z15 contain 6.4 ± 0.5 at% Ca. ZrO_2 is reported as a "lime sponge" in spinel- and MgO-containing refractories.[31,35] This can prevent formation of a low-melting interparticle film of glass or crystalline phase, which both reduce HMOR, and is a critical factor for RH degasser snorkel and lower vessel performance. Since there is a direct relationship between HMOR and erosion resistance,[12,14] the spinel-periclase-15% ZrO_2 composition is expected to give a better erosion resistance. This needs to be verified by testing and application trials. Overall, ZrO_2 addition enhances the HMOR of SP composition which is related to an overall reduction in the weight fraction of liquid phase at 1500°C, as predicted by FactSage (Figure 10).

Composition SP exhibited better thermal shock resistance compared to the zirconia-bearing compositions as evident from the high residual strength (Figure 13) after thermal cycling despite having a low apparent porosity (12.7%) which is expected to reduce thermal shock resistance.[54] This can be attributed to the fracture porosity at matrix-periclase interfaces (Figure 14). Thermal shock induced cracks up to 491 μm long were believed to be stopped when they intersected this fracture porosity around the periclase particles. Existence of fracture porosity was not observed in Z10 (Figure S1) probably due to the low thermal expansion mismatch between the ZrO_2-containing matrix and periclase

particles. But formation of large cracks was observed after thermal shock at the interface of matrix regions with heterogenous distribution of ZrO_2 (Figure 15). No substantial increase in intraparticle cracks among ZrO_2 particles was observed compared to the sintered one. This means that the individual cubic ZrO_2 particles, despite their low thermal shock resistance (reported ΔT is 100-150°C)[50], were not responsible for thermal shock failure of the spinel-periclase compositions. However, their collective presence as heterogenous ZrO_2-rich areas with higher thermal expansion coefficient generated cracks at the interface. Hence, the MOR after thermal shock (residual strength) of Z10, 2.7 MPa, was half of that of SP, 5.9 MPa (Figure 13). These ZrO_2-rich regions could be eliminated by ball milling the matrix (<90 μm powder) separately before mixing it with coarse and medium particles.

Slag corrosion resistance of spinel-periclase compositions should theoretically increase with ZrO_2 addition[25,30] because ZrO_2 can react with CaO in the penetrating slag and form a "slag barrier", containing high melting point phases like $CaZrO_3$ (T_m is 2314°C).[38] However, in this experiment such improvement was not observed. It is important to note that pore diameter (Figure 17) of SP was the smallest (9.87 μm), and it gradually increased with ZrO_2 addition till Z7.5 (19.65 μm) after which it reduced. The reasons for this change of pore size with ZrO_2 addition and methods to mitigate the same were discussed earlier. Overall it seems that the slag penetration depth increased with increasing pore size in Figure 17 which is in accordance with the Washburn model (Equation 2) for liquid penetration into a capillary:[55,56]

$$h^2 = \frac{r(\cos\theta)\sigma t}{2\eta}, \tag{2}$$

where, h is the slag penetration depth, r the pore radius, θ the contact angle, σ the surface tension, t the interaction time, and η the slag viscosity. The apparent porosity (volume fraction of open pores) on the other hand decreased with ZrO_2 addition (Figure 8) and only Z15 had slightly higher porosity (13.4%) than SP (12.7%). Hence, pore size had a much greater impact on slag penetration than the volume fraction of open pores here, an idea commonly accepted by the refractory ceramics community. In fact, if the equilibrium contact angle of slag (θ) is higher than 90°, a minimum threshold pore radius r^*[57]given in Equation (3) exists such that if the pore size of the refractory is below r^*, the slag cannot penetrate, regardless of the volume fraction of open pores.

$$r* = -\frac{2\sigma\cos\theta}{\rho g l}, \tag{3}$$

where ρ is the density of liquid slag, l the depth of liquid slag layer on the refractory, and g the acceleration due to gravity.

The slag is rich in FeO_x in the RH degrasser, and FeO_x is considered especially detrimental because of its ability to form eutectic phases with a wide range of refractory oxides, with the corrosion aggravated by additional presence of MnO_x and SiO_2. In the region of high Fe concentration in the Fe map (Figure 18), Fe is seen to equally corrode MgO and spinel. The MgO-FeO phase diagram[58] shows complete solid solubility of FeO in MgO, and the melting point decreases with such substitution. Both FeO and Fe_2O_3 have a significant solubility in spinel.[35,59,60] If Fe is taken up in the MgO solid solution, the viscosity of the infiltrating slag might increase, reducing its penetration into the refractory. The elemental map of Fe in SP (Figure 19) shows significant penetration in case of spinel matrix and sintered MgO except for fused MgO. This proves the higher corrosion resistance of fused MgO compared to that of sintered MgO. The high corrosion resistance of the fused MgO particle is due to the lack of grain boundaries as these particles are made up of large 500 μm grains as compared to the 80 μm grain size in sintered MgO. A representative microstructure of a fused MgO particle in Z15 is shown in Figure S2. The thermodynamic equilibrium calculation on interaction between SP and RH slag also points toward the resistance of MgO to slag in comparison with spinel (Figure 20), and attributes it to the higher solubility of Al_2O_3 in slag. The MgO phase is not only stable in slag, but it takes up FeO_x into the solid solution. Due to the large Al_2O_3 pick up and loss of FeO_x, the viscosity of RH degasser slag was predicted to increase from 0.2 poise to 1 poise as it continued infiltrating into SP composition. This might hinder slag penetration. Since Fe is the most corrosive element, mitigation of FeO_x penetration should be a priority to enhance corrosion resistance. This leads to another inference about the choice of refractory raw materials for spinel-periclase refractories for application in a RH degasser. The order of decreasing corrosion resistance is fused MgO, sintered MgO, and MR66 sintered spinel. Hence, if the RH degasser slag in a steel plant is rich in FeO_x, the fused MgO as well as overall MgO:spinel ratio in the brick might be increased. However, the thermal shock resistance may get adversely impacted due to increase in fused MgO in the composition[34] which needs to be evaluated.

Fused MgO demonstrates much higher corrosion resistance than the matrix infused with 10% ZrO_2 in case of Z10 after interaction with slag (Figure 21). Contrary with the popular belief that ZrO_2 addition increases corrosion resistance of refractories made from MgO and spinel, it is observed here that the large fused MgO particles have a higher corrosion resistance than fused ZrO_2, in situ spinel, presintered MR66 spinel and sintered MgO, which were all present in the matrix. It might be interesting to study the impact of fused ZrO_2 having a larger particle size on properties of spinel-periclase refractories. Since fused MgO has a higher corrosion resistance than the ZrO_2-infused

matrix, the deterioration of slag corrosion resistance of spinel-periclase refractories due to ZrO_2 addition might also be caused due to a lower fused MgO content. SP and Z15 contain 25% and 21.25% fused MgO, respectively, which was chosen to maintain 1:1 ratio between fused and sintered MgO (Table 2). The EDS analysis of ZrO_2 particles in slag corroded Z10 (Figure 22) shows that the Mg/Ca ratio decreases from 1.35 before slag corrosion (Table S1) to 0.64 after corrosion (Table 4), and some of the Mg^{2+} already present in the ZrO_2 particles are substituted by Ca^{2+} from slag. The overall uptake of Ca^{2+} in the ZrO_2particles (Ca/(Ca + Mg+Zr) ratio) doubles to 0.14 during corrosion. In Z10, the ZrO_2 particles also absorb Fe from the slag (increase of 3.8 at%). Ceylantekin and Aksel[30] had added $ZrSiO_4$ to spinel-periclase refractory and found that ZrO_2(formed from decomposition of $ZrSiO_4$ during sintering) reacted with CaO from the slag forming $CaZrO_3$, which acted as a "barrier" to further slag penetration. In Figure 22, the Fe content is seen to reduce from 74.7% (F1) near the slag region to 11.7% (F2) behind the "slag barrier" formed by the high Ca-containing cubic ZrO_2 (Z) and $CaZrO_3$ (X1 and X2) particles.

The calculated Fe content in the MgO and spinel solid solutions is similar in both Z10 and SP (Tables 4 and S2), but the measured values by EDS shows that both spinel and MgO phases in SP take up more Fe into solid solution than in Z10. This could make the penetrating slag more viscous in the case of SP, leading to reduced slag corrosion. The formation of $CaZrO_3$ phase was not predicted when the bulk composition Z10 was equilibrated with RH slag (Figure 23A) due to the high Al_2O_3 content in the infiltrating slag originating from the spinel dissolution. Given that complete and instant equilibrium reactions between all phases in the refractory and the slag are unlikely during the experiments, direct interactions between cubic ZrO_2particles and the RH slag were also simulated in Figure 23D. The initial composition of the ZrO_2particles in the calculations was taken from Table S1. In this case, $CaZrO_3$ became a stable phase due to the high concentration of CaO in the slag. This corroborates the presence of $CaZrO_3$ in SEM-EDS analysis (Figure 22). The simulations also predicted a good stability of cubic ZrO_2 and supported the measured EDS data showing an increase in the Ca/Mg ratio in the cubic ZrO_2 phase before and after interaction with the RH slag. The cubic ZrO_2 composition after slag corrosion of Z10 is indicated on the ternary phase diagram by a red filled square marker in Figure 5. The evolution of the cubic ZrO_2 phase composition before and after slag corrosion (from black filled square marker to red filled square marker in Figure 5) demonstrates that the presence of the CaO-rich RH slag caused the cubic ZrO_2 composition to move toward the CaO corner of the phase diagram due to CaO intake, where the $CaZrO_3$ phase becomes stable.

Overall, it can be inferred that pore size has a strong effect on corrosion resistance (Figure 17).Despite obstruction of slag penetration locally by the added ZrO_2 which forms a slag barrier (cubic ZrO_2 + $CaZrO_3$), the overall corrosion resistance was not improved due to the larger pore size and lower FeO_x uptake by the spinel and periclase phases. Z15 showed a better corrosion resistance among the ZrO_2-containing spinel-periclase refractories. Considering the wide variation in RH degasser slag chemistry and thermal regimes in different steel plants all over the world, this detailed correlation among raw material chemistry, ceramic processing, thermomechanical properties, and corrosion resistance might enable engineering of commercially viable environment-friendly Cr-free refractories.

5 | CONCLUSIONS

This study clearly demonstrates that through a judicious choice of raw materials, designing of particle size distribution and proper processing, it is possible to create chrome-free refractories meeting the stringent property requirement for RH Degasser lower vessel and snorkel application. Proper aggregate size design helped in achieving a spinel-periclase refractory having 14 wt% in situ spinel content with an apparent porosity and mean pore diameter of 12.7% and 9.87 μm respectively. The porosity further decreased to 11% with ZrO_2 addition of 5 wt%, which is close to the lower range of the reported porosity for direct-bonded magnesia-chrome refractories. Addition of ZrO_2 increased the hot strength and the 15 wt% ZrO_2-bearing composition exhibited an HMOR of 7.2 MPa. The stabilization of ZrO_2 from monoclinic to cubic phase by taking in Mg^{2+} and Ca^{2+} ions from the matrix, confirmed by XRD, resulting in reduction of liquid phase formation as demonstrated by FactSage calculations, could be the reason for this. The elemental maps of the SP composition after interaction with RH slag clearly shows the resistance of fused large grain magnesia against FeO_x attack thus improving the corrosion resistance. Although the cubic zirconia absorbed more calcium ions from the slag potentially altering its viscosity, the ZrO_2 added compositions showed inferior slag corrosion resistance and higher slag penetration owing to larger mean pore diameter. The increased lime pickup and the formation of $CaZrO_3$ as predicted by FactSage calculations have been confirmed experimentally. Further optimization of the ZrO_2 particle size and its uniform distribution in the matrix is essential to reduce the mean pore diameter as well as prevent micro-crack generation in zirconia-containing composition during cycling. A chrome-free refractory with good slag corrosion resistance and thermal shock resistance for RH Degasser snorkel and lower vessel can thus be created.

ACKNOWLEDGMENTS

Somnath Mandal is thankful for the Indian Ministry of Human Resource Development Scholarship (2013-2015), the Indian Science and Engineering Research Board Overseas Doctoral Fellowship (SERB-UCI, 2017-2020), the ASTM International Graduate Scholarship (2019) and The Refractories Institute Scholarship (2019). Sarah Finkeldei and William Bowman acknowledge the University of California, Irvine (UCI) new-faculty setup funding. The authors appreciate Martha Mecartney (UCI) for helpful comments on the manuscript and for partially supporting some experiments by NSF DMR 1611457. Most SEM-EDS analyses were conducted using the TEM facility at the Irvine Materials Research Institute (UCI). The authors are grateful to Shankha Chatterjee and Sarbapi Mukherjee (Almatis Alumina Pvt. Ltd., India) for providing free samples of MR66 spinel, P. Abdul Rasheed and Soney Varghese for assistance with SEM analysis done at the National Institute of Technology Calicut, India, and the staff at the laboratory of TRL Krosaki Refractories Limited for experimental assistance. The authors greatly appreciate comments on the manuscript from Regina Ragan (UCI).

ORCID

Somnath Mandal https://orcid.org/0000-0003-1021-8786
C. J. Dileep Kumar https://orcid.org/0000-0002-9129-4766
Devendra Kumar https://orcid.org/0000-0003-4549-6444
In-Ho Jung https://orcid.org/0000-0002-9744-7276
Sarah C. Finkeldei https://orcid.org/0000-0002-1943-0604
William J. Bowman https://orcid.org/0000-0002-4346-1144

REFERENCES

1. Eichert T, Meier-Kortwig J, Tembergen D, Heiligenbrunner M, Maranitsch A. Latest concepts for RH-degassers and their refractory linings. In: Smith JD, Schmidt-Whitley R, editors. Proceedings of the Unified International Technical Conference on Refractories. Dresden, Germany: German Refractories Association; 2007. p. 69–72.
2. Van Ende MA, Kim YM, Cho MK, Choi J, Jung IH. A kinetic model for the Ruhrstahl Heraeus (RH) degassing process. Metall Mater Trans B. 2011;42:477–89.
3. Cho MK, Van Ende MA, Eun TH, Jung IH. Investigation of slag-refractory interactions for the Ruhrstahl Heraeus (RH) vacuum degassing process in steelmaking. J Eur Ceram Soc. 2012;32(8):1503–17.
4. Grand View Research. Automotive steel market size, share & trends analysis report by application (body structure, power train, suspension), by vehicle type (LCVs, HCVs), by region, and segment forecasts, 2019–2025. https://www.grandviewresearch.com/industry-analysis/automotive-steel-market. Accessed July 27, 2020
5. World Steel Association. World steel in figures 2019. https://www.worldsteel.org/en/dam/jcr:96d7a585-e6b2-4d63-b943-4cd9ab621a91/World%2520Steel%2520in%2520Figures%25202019.pdf. Accessed July 27, 2020
6. Lee WE, Moore RE. Evolution of in situ refractories in the 20th century. J Am Ceram Soc. 1998;81(6):1385–410.
7. IndustryARC. Global refractories market value breached $25.4 billion in 2018. https://www.IndustryARC.com/PressRelease/1172/Refractories-Market-Research.html. Accessed July 27, 2020
8. IndustryARC. Lithium ion battery market—forecast (2020–2025). https://www.IndustryARC.com/Report/15433/lithium-ion-battery-market.html. Accessed July 27, 2020
9. Tassot P, Verrelle D, Vromen C. Recent developments & performance from RHOB at Sollac Dunkirk. In: Stett MA, editor. Proceedings of the Unified International Technical Conference on Refractories. New Orleans, LA: The American Ceramic Society; 1997. p. 223–30.
10. Martino M, Curletto L, Bonifacino V. Some correlations between composition and characteristics in the field of chrome-free refractories for steel degassing. Paper presented at the Unified International Technical Conference on Refractories; November 4–7, 2001; Cancun, Mexico.
11. Ishii H, Kanatani S, Sasaki K, Okamoto T, Aida K. Improvement of magnesia-carbon brick for lower vessel of RH-degassing. In: Yamato T, Nishio H, editors. Proceedings of the Unified International Technical Conference on Refractories. Osaka, Japan: Technical Association of Refractories, Japan; 2003. p. 114–7.
12. Andersen F, Schmidt A, Van Der LS. RH degassers; evaluation and ranking of eco-refractories. In: Yamato T, Nishio H, editors. Proceedings of the Unified International Technical Conference on Refractories. Osaka, Japan: Technical Association of Refractories, Japan; 2003. p. 110–3.
13. Czapka Z, Skalska M, Zelik W. Mechanisms of wear of refractory materials in snorkels of RH degasser and the possibilities for their reduction. In: Smith JD, editor. Proceedings of the Unified International Technical Conference on Refractories. Orlando, FL: The American Ceramic Society; 2005. p. 19–23.
14. Bi Y, Smith IA, Andreev K. Development of degasser snorkel refractories and the effect of the process parameters on wear rate. In: Goski DG, Smith JD, editors. Proceedings of the Unified International Technical Conference on Refractories. Victoria, BC, Canada: The American Ceramic Society; 2013. p. 755–9.
15. Tsuchinari A, Osaki H, Okamoto H, Yamamoto T, inventors. Harima Ceramic Co., Ltd., assignee. Chrome-free brick. United States Patent 5559064. Sep 24, 1996. https://patentimages.storage.googleapis.com/8a/5c/de/9dc8a41377e888/US5559064.pdf. Accessed July 27, 2020
16. Bray DJ. Toxicity of chromium compounds formed in refractories. Am Ceram Soc Bull. 1985;64(7):1012–6.
17. Müller M, Hilpert K, Singheiser L. Corrosion behaviour of chromium-free ceramics for liquid slag removal in pressurized pulverized coal combustion. J Eur Ceram Soc. 2009;29(13):2721–6.
18. Petkov V, Jones PT, Boydens E, Blanpain B, Wollants P. Chemical corrosion mechanisms of magnesia-chromite and chrome-free refractory bricks by copper metal and anode slag. J Eur Ceram Soc. 2007;27(6):2433–44.
19. Goto K, Argent BB, Lee WE. Corrosion of MgO-$MgAl_2O_4$spinel refractory bricks by calcium aluminosilicate slag. J Am Ceram Soc. 1997;80(2):461–71.

20. Rai D, Eary LE, Zachara JM. Environmental chemistry of chromium. Sci Total Environ. 1989;86(1-2):15–23.
21. Hausladen DM, Alexander-Ozinskas A, McClain C, Fendorf S. Hexavalent chromium sources and distribution in California groundwater. Environ Sci Technol. 2018;52(15):8242–51.
22. Shimizu K, Hokii T, Asano K, Miki T. Chrome-free brick applied to lower vessel of RH degasser. In: Yamato T, Nishio H, editors. Proceedings of the Unified International Technical Conference on Refractories. Osaka, Japan: Technical Association of Refractories, Japan; 2003. p. 118–21.
23. Mati APDM, Goncalves GE, Soares SE, Lara GI, Almeida END, Brito MADM. RH degassers operational conditions in Brazil, a challenge for refractory. In: Tsukamoto N, Kayama T, editors. Proceedings of the Unified International Technical Conference on Refractories. Kyoto, Japan: UNITECR2011; 2011:p. 317–20.
24. Mandal S, Dileep Kumar CJ, Adak S, Kumar D, Chattopadhyay AK. Phase evolution, microstructure and thermo-mechanical characteristics of titania bearing spinel-periclase refractories for RH degasser. Paper presented at the Unified International Technical Conference on Refractories; September 17, 2015; Vienna, Austria.
25. Obana T. Trend of chrome-free refractory materials. J Tech Assoc Refract Jpn. 2010;30(4):243–9.
26. Schacht CA, editor. Refractories handbook. New York, NY: Marcel Dekker; 2004.
27. Lodha R, Ghosh A, Mukherjee B, Agrawal GN. Zirconia-magnesium aluminate spinel composite. Am Ceram Soc Bull. 2006;85(6):9201–3.
28. Ceylantekin R, Aksel C. Improvements on the mechanical properties and thermal shock behaviours of MgO-spinel composite refractories by ZrO_2 incorporation. Ceram Int. 2012;38(2):995–1002.
29. Mohan SK, Sarkar R. Effect of ZrO_2 addition on $MgAl_2O_4$ spinel from commercial grade oxide reactants. Ceram Int. 2016;42(8):10355–65.
30. Ceylantekin R, Aksel C. Improvements on corrosion behaviours of MgO-spinel composite refractories by addition of $ZrSiO_4$. J Eur Ceram Soc. 2012;32(4):727–36.
31. Gruver SP, inventor; Baker Refractories, assignee. Magnesia spinel refractory brick. United States Patent 6261983B1. Jul 17, 2001. https://patentimages.storage.googleapis.com/7c/35/dc/b9c8630832c0fc/US6261983.pdf. Accessed July 27, 2020
32. Guo Z, Palco S, Rigaud M. Reaction characteristics of magnesia-spinel refractories with cement clinker. Int J Appl Ceram Technol. 2005;2(4):327–35.
33. Sarkar R, Sahoo S. Effect of raw materials on formation and densification of magnesium aluminate spinel. Ceram Int. 2014;40(10B):16719–25.
34. Suruga T, Hatae E, Yoshitomi J, Asano K, Yamato T. Effect of MgO aggregate on the thermal characteristics of magnesia-spinel bricks. J Tech Assoc Refract Jpn. 2002;22(2):126–31.
35. Mandal S, Mondal S, Das K. Microstructure and phase evolution of Indian magnesite-derived $MgAl_2O_4$ as a function of stoichiometry and ZrO_2 doping. Int J Appl Ceram Technol. 2018;15(1):161–70.
36. Tassot P, König G, Seifert F, Liebau F. Subsolidus, high temperature phase relations in the systems Al_2O_3-Cr_2O_3-ZrO_2, MgO-Cr_2O_3-ZrO_2 and MgO-Al_2O_3-ZrO_2. J Mater Sci. 1986;21(10):3479–82.
37. Duwez P, Odell F, Brown FHJ. Stabilization of zirconia with calcia and magnesia. J Am Ceram Soc. 1952;35(5):107–13.
38. Kwon SY, Jung IH. Critical evaluation and thermodynamic optimization of the CaO-ZrO_2 and SiO_2-ZrO_2 systems. J Eur Ceram Soc. 2017;37(3):1105–16.
39. Pavlyuchkov D, Savinykh G, Fabrichnaya O. Experimental investigation and thermodynamic modeling of the ZrO_2-MgO system. Adv Eng Mater. 2013;15(7):618–26.
40. Anderson PJ, Horlock RF. Thermal decomposition of magnesium hydroxide. Trans Faraday Soc. 1962;58(478):1993–2004.
41. Martens R, Gentsch H, Freund F. Hydrogen release during the thermal decomposition of magnesium hydroxide to magnesium oxide. J Catal. 1976;44(3):366–72.
42. ASTM. C830–00 Standard test methods for apparent porosity, liquid absorption, apparent specific gravity, and bulk density of refractory shapes by vacuum pressure. West Conshohocken, PA: ASTM International; 2016.
43. ASTM. C133–97 Standard test methods for cold crushing strength and modulus of rupture of refractories. West Conshohocken, PA: ASTM International. 2015.
44. ASTM. C1171–16 Standard test method for quantitatively measuring the effect of thermal shock and thermal cycling on refractories. West Conshohocken, PA: ASTM International; 2016.
45. Ghosh C, Ghosh A, Haldar MK. Studies on densification, mechanical, micro-structural and structure-properties relationship of magnesium aluminate spinel refractory aggregates prepared from Indian magnesite. Mater Charact. 2015;99:84–91.
46. Bale CW, Bélisle E, Chartrand P, Decterov SA, Eriksson G, Gheribi AE, et al. FactSage thermochemical software and databases, 2010–2016. CALPHAD Comput Coupling Phase Diagrams Thermochem. 2016;54:35–53.
47. Cunha-Duncan FN, Bradt RC. Synthesis of magnesium aluminate spinels from bauxites and magnesias. J Am Ceram Soc. 2002;85(12):2995–3003.
48. Jeschke P. Texture analysis of basic refractory brick. J Am Ceram Soc. 1966;49(7):360–3.
49. Coble RL, Kingery WD. Effect of porosity on physical properties of sintered alumina. J Am Ceram Soc. 1956;39(11):377–85.
50. Angle JP, Steppan JJ, Thompson PM, Mecartney ML. Parameters influencing thermal shock resistance and ionic conductivity of 8 mol% yttria-stabilized zirconia (8YSZ) with dispersed second phases of alumina or mullite. J Eur Ceram Soc. 2014;34(16):4327–36.
51. Luo J, Stevens R. Porosity-dependence of elastic moduli and hardness of 3Y-TZP ceramics. Ceram Int. 1999;25(3):281–6.
52. Maca K, Pouchly V, Zalud P. Two-step sintering of oxide ceramics with various crystal structures. J Eur Ceram Soc. 2010;30(2):583–9.
53. Yan W, Li N, Li Y, Liu G, Han B, Xu J. Effect of particle size on microstructure and strength of porous spinel ceramics prepared by pore-forming in situ technique. Bull Mater Sci. 2011;34(5):1109–12.
54. Shen L, Liu M, Liu X, Li B. Thermal shock resistance of the porous Al_2O_3/ZrO_2 ceramics prepared by gelcasting. Mater Res Bull. 2007;42(12):2048–56.
55. Mukai K, Tao Z, Goto K, Li Z, Takashima T. In-situ observation of slag penetration into MgO refractory. Scand J Metall. 2002;31(1):68–78.
56. Einset EO. Capillary infiltration rates into porous media with applications to silcomp processing. J Am Ceram Soc. 1996;79(2):333–8.
57. Poirier J, Smith JD, Jung IH, Kang YB, Eustathopoulos N, Blond E, et al. Corrosion of refractories: the fundamentals. Baden-Baden, Germany: Goller Verlag GmbH; 2017.
58. Wu P, Eriksson G, Pelton AD, Blander M. Prediction of the thermodynamic properties and phase diagrams of silicate systems-evaluation of the FeO-MgO-SiO_2 system. ISIJ Int. 1993;33(1):26–35.
59. Jacob KT, Patil R. Activities in the spinel solid solution $Fe_xMg_{1-x}Al_2O_4$. Metall Mater Trans B. 1998;29(6):1241–8.

60. Kwestroo W. Spinel phase in the system MgO-Fe_2O_3-Al_2O_3. J Inorg Nucl Chem. 1959;9:65–70.

SUPPORTING INFORMATION

Additional supporting information may be found online in the Supporting Information section.

How to cite this article: Mandal S, Dileep Kumar CJ, Kumar D, et al. Designing environment-friendly chromium-free Spinel-Periclase-Zirconia refractories for Ruhrstahl Heraeus degasser. *J Am Ceram Soc*. 2020;00:1–20. https://doi.org/10.1111/jace.17402